

THESIS

DESIGN AND SIMULATION OF THE COLORADO STATE UNIVERSITY
LINEAR ACCELERATOR SYSTEM

Submitted by

Jonathan Paul Edelen

Department of Electrical and Computer Engineering

In partial fulfillment of the requirements

For the Degree of Master of Science

Colorado State University

Fort Collins, Colorado

Fall 2014

Master's Committee:

Advisor: Stephen Milton
Co-Advisor: Sandra Biedron

Branislav Notaros
Thomas Johnson

Copyright by Jonathan Paul Edelen 2014

All Rights Reserved

ABSTRACT

DESIGN AND SIMULATION OF THE COLORADO STATE UNIVERSITY LINEAR ACCELERATOR SYSTEM

The University of Twente in the Netherlands recently donated a linear accelerator and free-electron laser system to Colorado State University. A detailed model and simulation of the system must be constructed in order to assist the re-commissioning process at CSU. An initial design of the beam-transport system must also be developed. This thesis begins with the basic theory needed to understand the context of the simulations and then works through the accelerator, starting from the point where the beam is generated and continuing through the whole system to the beam dump. Individual components are simulated, their parameters are characterized, and optimal initial settings are found. These individual simulations are then combined into a complete start-to-end simulation of the machine. The start-to-end simulation is then used to demonstrate the expected performance of the machine with the optimal settings. This provides a system design that will be used in the initial buildup of the accelerator, as well as a simulation tool that can be used for future studies (for example, testing of novel components) or for examining the impact of proposed design changes.

TABLE OF CONTENTS

ABSTRACT.....	ii
LIST OF TABLES.....	v
LIST OF FIGURES.....	vi
1. Introduction.....	1
2. Linear Accelerator Design Theory.....	5
2.1 Particle acceleration and radio frequency accelerating structures.....	5
2.1.1 A simple RF accelerator: the pill-box cavity.....	6
2.1.2 Coupled cavity linear accelerators.....	8
2.1.3 RF particle acceleration.....	11
2.2 Electron beam properties.....	13
2.2.1 Beam phase space and emittance.....	13
2.2.2 Statistical definition of emittance for 2-D phase space.....	16
2.3 Beam dynamics in the RF accelerator and emittance growth effects.....	17
2.3.1 RF effects on emittance.....	17
2.3.2 Space charge effects on emittance.....	21
2.4 Beam transport and matching.....	24
3. Electromagnetic Modeling of the Colorado State University Linear Accelerator.....	29
3.1 The Colorado State University linear accelerator.....	29
3.2 Modeling of the RF linear accelerator.....	30
3.3 The solenoid and bucking coil assembly.....	38
3.4 LINAC measurements and data analysis.....	41
4. Characterization of the RF Linear Accelerator.....	46
4.1 PARMELA beam dynamics calculations and sensitivity analysis.....	46
4.1.1 Sensitivity to number of particles (without space charge).....	47
4.1.2 Sensitivity to integration step (without space charge).....	48
4.1.3 Sensitivity to space charge routine parameters.....	49
4.1.4 Sensitivity to number of particles and phase step with space charge.....	51
4.2 Injector simulation studies.....	52
4.2.1 RF Phase effects.....	53
4.2.2 Solenoid focusing and beam charge effects on emittance.....	55
4.2.3 Cathode spot size effects on emittance.....	58
4.2.4 Bunch length effects on emittance.....	59
4.3 Injector point design.....	61
5. Beam-Line Matching for the Undulator.....	63
5.1 Overview of eL_{egant} and TR_ACE-3D.....	64
5.2 Beam-line Matching to the Undulator.....	65
5.3 Matching sensitivity to input beam parameters.....	73
6. Spectrometer Diagnostic Optimization.....	76
7. Start to end beam simulations and startup layout.....	80

References	87
Appendix A: SUPERFISH Cavity Input Files	88
A.1 Cell-1	88
A.2 Cell-2	89
A.3 Cell-3	90
Appendix B: Solenoid Model	91
Appendix C: PARMELA Input File	93

LIST OF TABLES

Table 1: Definition of first two magnetic field components in the multi-pole expansion.....	25
Table 2: Quality factor and shunt impedance data computed for the three cell types by SUPERFISH.	37
Table 3: Los Alamos Measurements vs CSU measurements	44
Table 4: Beam parameters and injector parameters for a point design.....	61
Table 5: Twiss parameters at the exit of the injector for the point design provided.....	62
Table 6: Beam line elements and positions for the starting point to the elegant optimization	66
Table 7: RMS twiss parameter starting values and target values for the beam-line tuning in	66
Table 8: Comparison of Twiss parameters with TRACE and PARELA to the target values	69
Table 9: Twiss parameters at the entrance to the undulator from TRACE and PARMELA.....	69
Table 10: Beam parameters from PARMELA simulation with beam-line settings from iteration of TRACE and PARMELA	71
Table 11: Final beam parameters from custom PARMELA optimization routine.....	71
Table 12: Comparison of beam-line settings produced from TRACE iterations to full simulation optimization	72
Table 13: Pre and Post wiggler twiss parameters	72
Table 14: Beam-line set points and locations for the matched system. Note that the zero point of the beam line is the exit of the injector.	73
Table 15: Results from TRACE match for a large beta and a small matched alpha.	74
Table 16: Results from TRACE match for a large beta and a small/modest mismatched alpha..	74
Table 17: Results from TRACE match for a large/modest mismatched beta and a small matched alpha.....	75
Table 18: Results from TRACE match for a large/modest mismatch in beta and alpha	75
Table 19: Starting Points for the Post Undulator Lattice.....	77
Table 20: Post wiggler beam line settings.	79
Table 21: Beam-line locations and set points..	84

LIST OF FIGURES

Figure 1: System level layout of the accelerator system with key components highlighted.	2
Figure 2: System-level diagram of injector components.	3
Figure 3: Beam-line consisting of five equally spaced quadrupoles	3
Figure 4: 3-cell coupled oscillator circuit.	9
Figure 5: Relativistic energy gamma vs. position of a particle.....	12
Figure 6: Phase space ellipse diagram in the x-x' plane with important parameters highlighted. 15	15
Figure 7: Error in Equation 23 as a function of injection phase	21
Figure 8: Cross section view of the photo-injector system.....	30
Figure 9: Schematic of the coupling slots in the linear accelerator.	32
Figure 10: View of details not modeled during this characterization.	32
Figure 11: Detailed view of the three cavity cell types	33
Figure 12: Resonant frequency as a function of the mesh interval showing relative stability.	34
Figure 13: Cell type 1 geometry and field contour model with axial field map on the right	35
Figure 14: Cell type 2 geometry and field contour model with axial field map on the right.	35
Figure 15: Cell type 3 geometry and field contour model with axial field map on the right.	36
Figure 16: Comparison of the axial field map modeled with SUPERFISH	38
Figure 17: Solenoid assembly drawing.....	39
Figure 18: Numerical model of the Solenoid showing the axial field map	40
Figure 19: S11 measurement of the RF cavity from 1.25GHz to 1.365GHz.....	42
Figure 20: Detailed view of each mode.	43
Figure 21: Resonant Frequency and quality factor as a function of the mode numbers.....	44
Figure 22: Transverse and Longitudinal emittance as a function of the number of particles.....	48
Figure 23: Transverse and longitudinal emittance as a function of the integration step.	49
Figure 24: Transverse and longitudinal emittance as a function of the long mesh number.	50
Figure 25: Transverse and longitudinal emittance as a function of the transverse mesh number. 51	51
Figure 26: Transverse and longitudinal emittance as a function of the integration step.	51
Figure 27: Transverse and longitudinal emittance as a function of the number of particles	52
Figure 28: Variation of the transverse emittance as a function of the RF injection phase	54
Figure 29: Variation in the longitudinal emittance as a function if the injection phase	54
Figure 30: Transverse emittance as a function of the solenoid strength,.....	56
Figure 31: Minimum transverse emittance as a function of the bunch charge.	56
Figure 32: Longitudinal emittance as a function of the solenoid strength.....	57
Figure 33: Transverse emittance as a function of the cathode spot size.....	58
Figure 34: Longitudinal emittance as a function of cathode spot sizes	59
Figure 35: Longitudinal emittance as a function of the bunch length	60
Figure 36: Transverse emittance as a function of the bunch length	60
Figure 37: Comparison of the Twiss parameters for elegant and PARMELA.	67
Figure 38: Comparison of the Twiss parameters for TRACE and PARMELA.	68
Figure 39: Comparison of the Twiss parameters for TRACE and PARMELA.	70
Figure 40: Transverse beta functions in post wiggler beam-line.....	78
Figure 41: Transverse beta functions in post wiggler beam-line.....	78
Figure 42: Vertical (y) dispersion along the post wiggler beam-line.	79

Figure 43: Transverse beta functions as a function of position along the accelerator.....	80
Figure 44: Transverse alpha functions as a function of position along the accelerator.....	81
Figure 45: Transverse emittance functions as a function of position along the accelerator.....	82
Figure 46: Longitudinal emittance functions as a function of position along the accelerator.....	83

1. Introduction

During the fall of 2011, the University of Twente (Netherlands) generously donated a particle accelerator system to Colorado State University. This includes an 11-cell, coupled-cavity linear accelerator operating at 1.3 GHz, beam-line components and diagnostics, steering and corrector magnets, an undulator magnet, and a number of other peripheral components needed for the system to operate. Together these components will initially be used as a THz free-electron laser or FEL.

There are a number of essential items that are required to make an operational FEL. A FEL generates radiation through the interaction of a high-energy electron beam, a co-propagating electro-magnetic field, and a spatially oscillatory magnetic field. To generate the required magnetic field, an undulator (sometimes referred to as a wiggler) magnet is used. An undulator is a series of dipole magnets that produce a sinusoidal magnetic field along the beam axis. The transversely accelerated electrons then emit EM radiation at a fixed wavelength (this is the primary source of the co-propagating EM field). The wavelength of emission of radiation is related to the period of the undulator magnets, the normalized magnetic field strength, and the beam energy. The electron beam must be of high quality for the FEL to work, and therefore care must be taken in its creation. The high-energy electron beam is created, accelerated, and adjusted by the accelerator and beam-line. Changes to the accelerator and beam-line parameters can be made in order to optimize the performance of the FEL.

The first step in the process is the creation of electron bunches in the electron gun at the beginning of the accelerator system. The bunches are generated through the use of the

photoelectric effect, which in this case is initiated by a laser pulse striking a cathode. High-power microwaves at a frequency of 1.3 GHz then accelerate these bunches to a kinetic energy of 6 MeV. After acceleration, the beam is manipulated and steered through the use of magnetic fields. This section, referred to as the beam-line, is used to match the beam parameters into the undulator. After exiting the undulator, the beam traverses an additional beam-line that is used to perform any further manipulation prior to being analyzed in the spectrometer and sent to the beam dump. A very basic schematic of this process is provided in Figure 1.

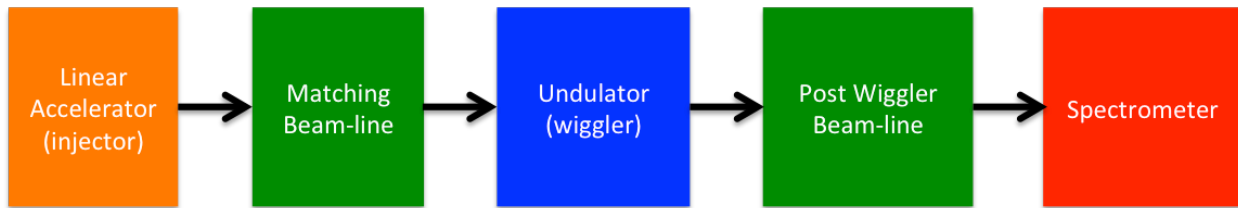


Figure 1: System level layout of the accelerator system with key components highlighted.

The coloring convention used in Figure 1 is the same convention that is used throughout this thesis. Orange denotes the injector system, green denotes the quadrupoles/beam transport system, blue denotes the undulator, and red denotes the spectrometer dipole. The two primary subsystems that are addressed in this thesis are the injector and the matching beam-lines. The first of these is the injector region given by Figure 2.

Here the electron beam is generated by a laser pulse (highlighted by a green dashed line) incident on the cathode stalk. The photoelectric effect then generates electrons that are accelerated via the standing wave cavities to 6 MeV. The solenoid and bucking coil serve to focus the beam during the initial acceleration and compensates for un-wanted beam effects.

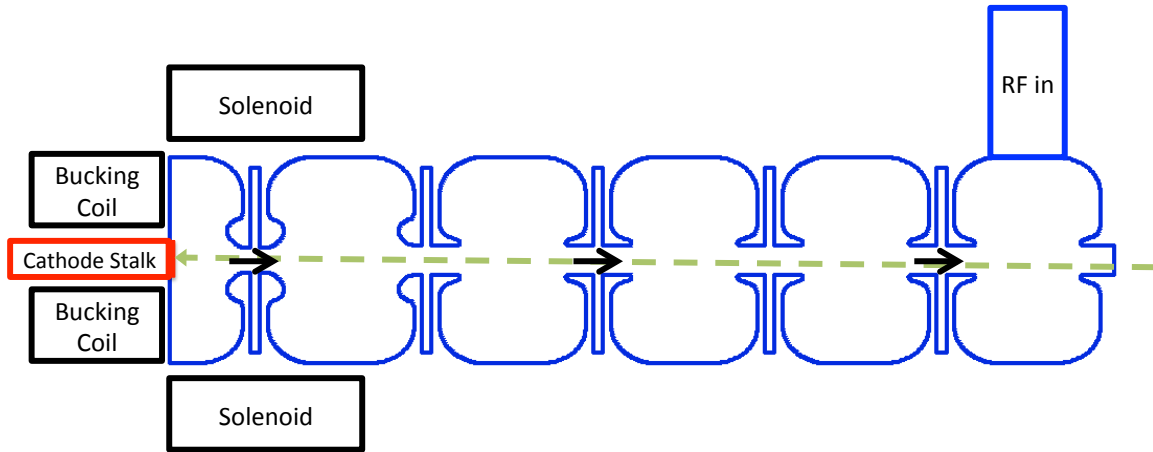


Figure 2: System-level diagram of injector components. Note the black arrows represent the beam and the green arrow represents the drive laser pulse.

Previously it was stated that the linear accelerator is an 11-cell structure; however, there are only 5.5 that are effectively excited and used for acceleration. The excited cells are the large cavities and the non-excited cells are the small gaps between the large cells. The purpose of these is discussed in Chapter 2. After the beam is accelerated, it is manipulated through the use of quadrupole lenses arranged as in Figure 3.



Figure 3: Beam-line consisting of five equally spaced quadrupoles

Here a simple beam-line layout is given, consisting of five equally spaced quadrupoles. Quadrupole fields are used to focus the beam and match the beam parameters to the undulator. These fields act on the beam similar to how an optical lens acts on visible light; however, changing the field strength can vary the focusing or defocusing properties of the quadrupole lens. Furthermore, a single quadrupole magnet is somewhat different than an optical lens in that although it focuses in one plane, say the horizontal, it defocuses in the orthogonal plane, say the

vertical. This represents, however, only a minor additional complication to the overall beam transport design. The details of this process are discussed in Chapter 2. The down-stream beam-line is of a similar configuration to Figure 3 but with only two quadrupoles.

This thesis begins by discussing important RF cavity parameters and how these cavities are used to accelerate electron beams. Following this, the important beam parameters are discussed. Then the beam dynamics during the injector are discussed, followed by a discussion on beam transport and focusing. Following the theoretical treatment, the linear accelerator system is modeled without the introduction of an electron beam, and the models as well as initial measurements of the rf-cavity system are reviewed in detail.

Following the analysis of the accelerating structure without the electron beam, full beam simulations are performed on the injector system. These simulations examine how the simulation parameters impact the accuracy of important beam calculations and how the system parameters change the beam dynamics inside the injector. The results and resulting simulated beam are then used to simulate the beam-line and match the beam parameters into the undulator. The matching under various operating conditions is also investigated to explore the robustness of the design. The post wiggler beam-line is also simulated to show how the beam evolves in this section of the accelerator. Following this, a full start-to-end simulation of the system is performed and the beam dynamics are analyzed. This then provides a system design that will be used in the initial buildup of the accelerator, as well as a simulation tool that can be used for future studies (for example, testing of novel components) or examining the impact of proposed design changes.

2. Linear Accelerator Design Theory

This chapter provides an overview of the necessary theory to explain how the accelerator system operates. To truly understand the nuances and complexities of the system, a detailed study of accelerators would be necessary; therefore, references are provided where necessary to indicate when the discussion is being cut short.

First, the basics of accelerating cavities without the introduction of a beam are discussed. This includes the important figures of merit and how a collective of cavities interact. This is followed by a discussion of how particles are accelerated. Next, the important beam properties are defined, followed by an analysis of the beam interactions with the RF acceleration fields, the beam self fields, and the external applied magnetic fields in the solenoid. It is useful to follow the work presented by Kim [1] when discussing RF and space charge effects on emittance. This chapter will reference this paper frequently as it is the primary reference for study of these effects. Finally, the various beam steering and focusing elements and how they change the beam parameters are discussed.

2.1 Particle acceleration and radio frequency accelerating structures

Particles can be accelerated using either electric or magnetic fields through the Lorentz force. In order to increase the kinetic energy of a particle, however, only electric fields can be used. The CSU accelerator utilizes standing-wave RF cavities for acceleration. In this section, the simplest standing wave RF cavity is discussed, followed by an introduction to the use of multi-cell structures, and, finally, a description of how the beam gains energy in an RF field is given.

2.1.1 A simple RF accelerator: the pill-box cavity

A pillbox cavity is an axially symmetric resonator commonly used for RF accelerators. Solving Maxwell's equations for the fields in a pillbox cavity gives an infinite number of modes that can be excited. The lowest order mode, TM_{010} , is often used for acceleration due to its relative simplicity. Out of the six possible field components, only two are present in this mode, and they are given by Equation 1a and 1b.

$$(1a) \quad E_z = E_0 J_0(k_r r) \cos \omega t$$

$$(1b) \quad B_\theta = \frac{E_0}{c} J_1(k_r r) \cos \omega t$$

Here E_0 is the peak electric field, k_r is the radial wave number, r is the radial distance from the cavity axis, and ω is the angular RF frequency. In this mode, the electric field only depends on the radial position and time. Because the electron beams are generated on-axis and have a small radius relative to the cavity, the small argument approximation for the Bessel function can be used, and thus the radial variation can be neglected. In a real accelerator there are additional components that introduce perturbations on those fields (e.g. beam-pipes, coupling slots, vacuum ports etc.), making these equations only an approximation, albeit a good one in most cases.

In order to accelerate the beam quickly, the peak field usually needs to be on the order of 10-20MV/m or greater. In the CSU accelerator, the peak field is about 26MV/m. In order to generate these fields, a great deal of power must be coupled into the cavity. Because there are power losses to the cavity walls, additional power is needed to sustain these fields. The quality factor Q , defined by the ratio of the stored energy to the dissipated energy in the cavity, is used to describe these losses. For a pillbox cavity without any additional complexities, the fields given by Equations 1a and 1b can be used to derive the result in Equation 2.

(2)

$$Q = \frac{2.405 \mu_0 c}{2\rho_s \left(1 + \left(\frac{R}{L}\right)\right)}$$

In this expression, 2.405 is the first zero of the zeroth-order Bessel function, μ_0 is the permeability of free space, ρ_s is the RF surface resistivity of the cavity, R is the cavity radius, and L is the cavity length. Equation 2 can provide estimates for the cavity Q of nominal dimension. Once the geometry is designed, simulation codes or measurements are required to obtain an accurate cavity Q. Another important cavity factor is the quantity of energy that can be delivered to the beam. Because the beam takes a finite amount of time to transit the cavity, the time varying component as well as the spatial varying component of the fields must be accounted for. The transit time factor is used to take this into account and is defined by Equation 3.

(3)

$$T = \frac{\int_{-\frac{L}{2}}^{\frac{L}{2}} E(0, z) \cos(\omega t(z)) dz}{\int_{-\frac{L}{2}}^{\frac{L}{2}} E(0, z) dz}$$

This expression holds true for an arbitrary spatially varying field in an arbitrary cavity driven at a given frequency. For a pillbox cavity in which the change in particle velocity across the gap is neglected, this expression can be simplified giving the result in Equation 4, where v is the particle velocity.

(4)

$$T = \frac{\sin\left(\frac{\omega L}{2v}\right)}{\frac{\omega L}{2v}}$$

The transit time factor, coupled with the geometry factors give rise to another important cavity parameter known as the shunt impedance. The shunt impedance is defined by the ratio of the squared energy gain per unit charge to the power delivered to the cavity. This describes in general how efficient the cavity is at delivering power to the beam. Equation 5 defines the shunt impedance for a pillbox cavity.

(5)

$$R_s = \frac{Z_0 L}{\pi \rho_s R} \frac{T^2}{\left(1 + \left(\frac{R}{L}\right)\right) J_1^2(2.405)}$$

Here the previously defined variables are the same, Z_0 is the impedance of free space, J_1 is the first-order Bessel function, and T is the transit time factor. These parameters are discussed in the context of the CSU accelerator in Chapter 3. For additional information and details on cavity design and cavity parameters, one can refer to a number of accelerator physics textbooks [1], [3], [4].

2.1.2 Coupled cavity linear accelerators

As mentioned previously, the CSU accelerator is an 11-cell coupled cavity structure. These structures can be analyzed using circuit models. To illustrate how a coupled-cavity structure operates, a 3-cell system is discussed. For a 3-cell system, the circuit model used is shown in Figure 3.

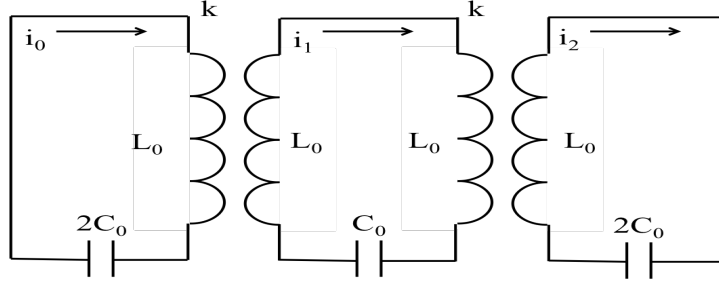


Figure 4: 3-cell coupled oscillator circuit. k is the coupling constant, L_0 is the cell inductance and C_0 is the cell capacitance.

Solving the circuit for the various loop currents yields a system of equations that describes how the circuit evolves. The result of this is illustrated by Equations 6a, 6b, and 6c.

(6a)

$$x_0 \left(1 - \frac{\omega_0^2}{\Omega^2} \right) + x_1 k = 0$$

(6b)

$$x_1 \left(1 - \frac{\omega_0^2}{\Omega^2} \right) + (x_0 + x_2) \frac{k}{2} = 0$$

(6c)

$$x_2 \left(1 - \frac{\omega_0^2}{\Omega^2} \right) + x_1 k = 0$$

Here x_n is the normalized current given by $x_n = i_n \sqrt{2L_0}$, k is the coupling constant, ω_0 is the resonant frequency of the uncoupled individual circuit components, i.e. $\omega_0 = 1/\sqrt{L_0 C_0}$, and Ω is the steady state oscillation frequency. In this circuit, the middle cell has twice the inductance as the outer two cells. To ensure the three cells have the same characteristic resonant frequency, the two outer cells have twice the capacitance as the inner cell. By writing Equations 6a, 6b, and 6c in a matrix form the eigenstates of the circuit can be solved. These eigenstates represent the individual modes that have steady-state oscillations. Equations 7, 8, and 9 show the normalized

current and steady-state oscillation frequency for the three modes. In these equations $X =$

$\begin{bmatrix} x_0 \\ x_1 \\ x_2 \end{bmatrix}$ and is the normalized current vector. The first mode, referred to as the zero-mode, has zero

phase shift between the cells.

(7)

$$\Omega_0 = \frac{\omega_0}{\sqrt{1+k}} \quad X = \begin{bmatrix} 1 \\ 1 \\ 1 \end{bmatrix}$$

The second mode has a 90-degree phase shift between the individual cells and is referred to as the pi/2 mode. The pi/2 mode is special in that the steady state frequency of the system is simply the resonant frequency. This is given explicitly in Equation 8.

(8)

$$\Omega_0 = \omega_0 \quad X = \begin{bmatrix} 1 \\ 0 \\ -1 \end{bmatrix}$$

The normalized current vector shows a clear 90-degree phase shift between cells. The final mode in the 3-cell system is the pi mode. Its normalized current and resonant frequency are given in Equation 9.

(9)

$$\Omega_0 = \frac{\omega_0}{\sqrt{1-k}} \quad X = \begin{bmatrix} 1 \\ -1 \\ 1 \end{bmatrix}$$

Here there is a clear 180-degree phase shift between the individual cells. Comparing equations 7, 8, and 9, reveals that there is something different about the pi/2 mode. Through the use of perturbation techniques, it can be shown that the pi/2 mode is a good mode to operate in because the power dissipation and cavity resonant frequency are much less sensitive to differences between the individual cell geometries. Detailed analysis of this is provided in [4]. The CSU

accelerator exploits the $\pi/2$ mode in an interesting way; the coupling cells are very small compared to the accelerating cells. This allows for the longitudinal field profile to look nearly continuous from the perspective of the beam instead of traversing zero-field regions. Additionally, through the impact of the transit time factor, a higher effective shunt impedance is achieved, thus improving the overall efficiency of the energy transfer to the beam. Expressed alternatively, and owing to the fact that the coupling cavities are much shorter than the accelerating cavities, the overall fields in the structure appear as a π -mode, but retain the favorable features of the $\pi/2$ mode.

2.1.3 RF particle acceleration

The π -like fields of the cavity can be exploited to do some initial calculations. These fields can be approximated as a sinusoidal time varying component with a cosine envelope function that takes into account the spatial variation of the fields along the cavity, Equation 10.

$$(10) \quad E_z = E_0 \cos(kz) \sin(\omega t + \phi_0)$$

Here, $k = 2\pi/\lambda$, and ϕ_0 is the injection phase of the particle relative to the RF waveform. A detailed analysis of how Equation 10 is used to describe the RF acceleration is given by Kim [2]. This analysis includes the derivation of concise analytical formulations that are useful in the initial accelerator design. For the purposes of showing how particles accelerate, Equation 10 is substituted into the Lorentz-force equation and solved numerically to produce the particle acceleration as a function of position in the cavity. This result is shown in Figure 5 for a given set of input parameters.

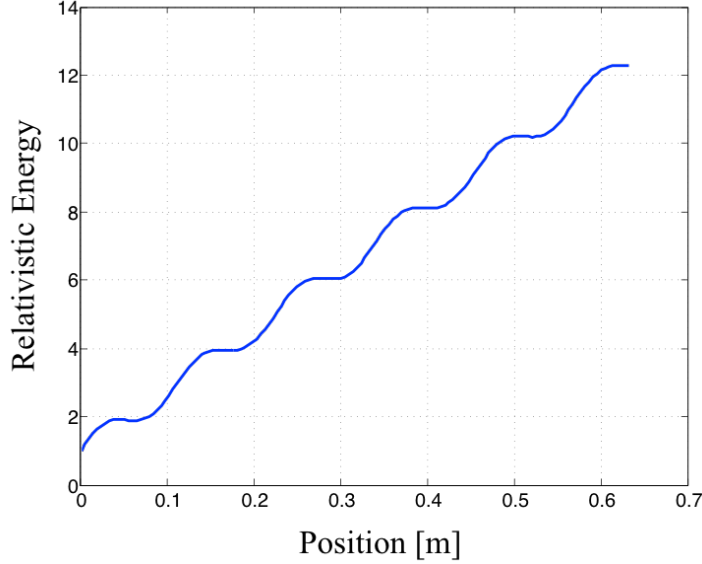


Figure 5: Relativistic energy gamma vs. position of a particle injected at 70 degrees relative to the RF fields, and an on-axis peak accelerating field of 20 MV/m.

This shows that as the particle transits the cavity, the variation in the fields lead to a ripple in the energy gain as a function of position. For a different injection phase, this ripple is exacerbated. The particle's phase is a quantity that takes into account the time varying field, the spatially varying field, and the relative injection phase of the particle. Equation 11 gives this definition.

$$(11) \quad \phi = \omega t + \phi_0 - kz$$

Using Equation 11 and Equation 10, a number of interesting relationships can be derived that relate the particle phase to the particle energy. Kim [1] shows this analysis extensively. One very important fact, one that will be used later when discussing longitudinal bunch dynamics, is the asymptotic phase limit of the particle, given by Equation 12.

(12)

$$\phi_\infty = \frac{1}{2\alpha \sin \phi_0} + \phi_0$$

Here ϕ_∞ is the asymptotic value of ϕ , i.e. the value that ϕ reaches upon completion of the acceleration cycle, and α is the normalized field strength given by $\alpha = qE_0/2mc^2k$, where q is

the fundamental unit of charge, E_0 is the peak electric field, m is the electron mass, c is the speed of light in vacuum, and k is the wave number of the fields.

2.2 Electron beam properties

Up to this point, only fields and single-particle motion have been considered. Later in this chapter, the discussion is expanded to collective effects in a particle beam. Before doing so, the parameters that are used to describe a particle beam are introduced. This will begin by discussing beam quality in the most general sense and be followed by an introduction to important parameters used to describe the 2-D phase space.

2.2.1 Beam phase space and emittance

For conservative systems, those that can be completely described by physical coordinates, canonical momentum, and time, Hamiltonian mechanics is used to explain their evolution. The term commonly used to describe the beam quality is called emittance. While there are many other measures of beam quality depending on the application, for the purposes of this thesis emittance is the primary concern. In the most general sense emittance is the volume that the electron beam occupies in 6-D phase space. The canonical momentum and position coordinates given for a Hamiltonian system define this 6-D space. Furthermore, it can be shown that this quantity is conserved in these systems [6].

It is very advantageous for accelerator design and operation to decouple the directions of motion as much as possible. This makes the calculations and beam manipulations simpler. At the CSU accelerator, a simple coordinate system where x and y are the transverse coordinates with phase or time as a longitudinal coordinate is adopted. In all cases, these coordinates are relative to the

electron bunch centroid. This gives phase spaces in the transverse planes, which are the $x-x'$ plane and the $y-y'$ plane, where x' and y' are the divergence coordinates of a particle given by $\frac{dx}{dz}$ and $\frac{dy}{dz}$ respectively, and effectively act in the role of the transverse momentum. Here z is the coordinate along the path of the bunch trajectory. The longitudinal phase space is composed of the phase and energy of the particles. Typically, energy and phase are treated as the deviation from a reference energy or phase that is the design energy or phase of the machine. The emittance in each plane can be described in terms of these variables.

At this point it helps to make an assumption that has significant impact on how we view the emittance. While, strictly speaking, the 6-D phase space is conserved, it can be quite unruly to measure this experimentally in a precise manner. Moreover, it is the core of the beam distribution that we are typically most interested in. As such, we generally compute the emittance by looking at second-order, rms values of the beam distribution. This allows us to make some useful simplifications, at the expense of noting that these quantities held separately and even taken together are not generally conserved. Nevertheless, historically this has proven to be a very valuable trade, as one now has a very powerful way of representing the beam in an analytical and satisfying fashion.

It is useful to look at the ellipse diagram shown in Figure 6. This shows how the emittance is computed and represented from an analytical perspective, as well as what beam properties emerge from the rms computed phase space.

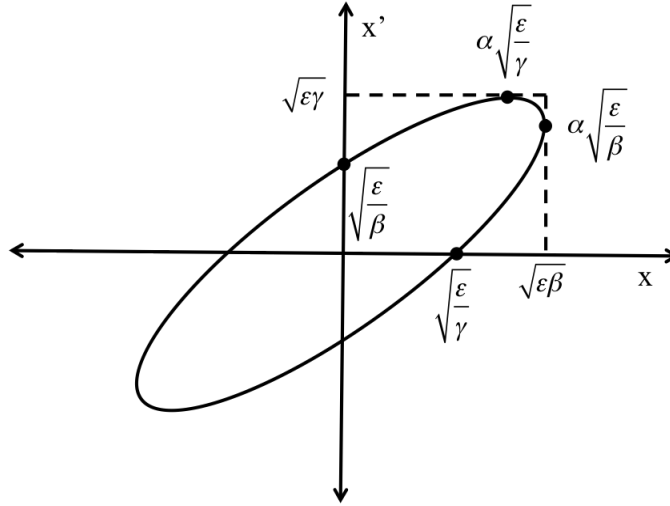


Figure 6: Phase space ellipse diagram in the $x-x'$ plane with important parameters highlighted

Here the emittance is represented by ϵ , and β and α can be viewed as the beam envelope function and the derivative of the beam envelope function, respectively. γ is a function of both α and β . These functions are referred to as the Twiss parameters, and they play heavily in particle beam design and transport. For an actual particle beam, there would be a collection of points in the phase space, one for each particle; however, when analyzing the bulk behavior, an ellipse serves very well to approximate the area in phase space occupied by these particles. That said, in a real beam there are often tails in the distribution (particles at very high phase space amplitudes) and higher order shapes, i.e. ones not readily characterized by RMS quantities, which exist in phase space. Such high amplitude particles or higher-order shapes are not easily manipulated and for the most part their existence does not affect the behavior of the beam RMS core distribution. When concerned with operating the FEL, the beam core distribution is the primary indicator, and the tails are ignored. This is where the introduction of a statistical definition of the beam parameters becomes important.

2.2.2 Statistical definition of emittance for 2-D phase space

For an ensemble of particles, we choose the following definitions for the longitudinal and transverse emittances respectively [7].

(13)

$$\epsilon_z = \frac{1}{n^2} \sqrt{\sum_n \Delta\gamma_i^2 \sum_n \Delta\phi_i^2 - \left(\sum_n \Delta\gamma_i\right)^2 \left(\sum_n \Delta\phi_i\right)^2}$$

(14)

$$\epsilon_x = \frac{1}{n^2} \sqrt{\sum_n x_i'^2 \sum_n x_i^2 - \left(\sum_n x_i' x_i\right)^2}$$

Here γ represents the particle relativistic energy, ϕ represents the particle phase, x represents the particle's longitudinal position, and x' represents the divergence in the transverse direction. These definitions will be used later in the context of explaining how various forces in the injector impact the emittance, and are used to compute the RMS Twiss parameters. The RMS emittances defined in equations 13 and 14 are used in conjunction with the RMS spot size in the beam phase space to define the RMS Twiss parameters.

(15a)

$$x_{rms} = \sqrt{\beta \epsilon_x}$$

(15b)

$$x_{rms} = \alpha \sqrt{\frac{\epsilon_x}{\beta}}$$

The RMS Twiss parameters are useful when studying the evolution of the core of the beam that will be important in later chapters.

2.3 Beam dynamics in the RF accelerator and emittance growth effects

The beam has two primary interactions in the accelerator region, the effects of external fields and the effects of the beam self-fields known as space-charge. These two effects are treated independently beginning with the effects of external fields. This section will follow closely the paper by Kim referenced earlier [ibid].

2.3.1 RF effects on emittance

The RF fields have an effect on both longitudinal and the transverse dynamics inside the linear accelerator. Some hint to the longitudinal effects was given earlier, but the meaning of this effect will be discussed in a bit more detail. Additionally, an introduction to how the RF fields affect the transverse bunch dynamics is also covered.

2.3.1.2 RF effects on longitudinal bunch dynamics

Following Kim, recall equation 12, which defined the asymptotic limit of the bunch phase relative to the injection phase. Suppose a perturbation was given to the initial phase; there would be some corresponding perturbation to the asymptotic phase. For a beam of finite phase width, this shows how much the asymptotic phase changes as a function of injection phase, thus showing the bunch either compresses or expands in phase. This gives rise to the so-called asymptotic bunch compression factor given by Equation 16.

(16)

$$\frac{d\phi_{\infty}}{d\phi_0} = 1 - \frac{\cos \phi_0}{2\alpha \sin^2 \phi_0}$$

Note that here α is referring to the normalized field strength defined earlier, not the α referred to in Figure 6. The asymptotic bunch compression factor is maximized for small injection phases. For a long bunch, such as that used by the CSU accelerator (~20 ps), the minimum injection

phase is about 10 degrees. Thus the shortest bunches should occur close to this minimum injection phase.

To analyze the effects of the RF field on the longitudinal emittance, a perturbation to the phase space area described in Equation 13 is introduced. This requires the help of Equation 17, which defines the relativistic energy in terms of the particle phase.

$$(17) \quad \gamma = 1 + \alpha[(n + 1/2)\pi \sin \phi + \cos \phi]$$

Introduction of a perturbation on the phase term and energy terms in Equation 16 gives rise to an expression, which can be approximated and substituted into the statistical definition for longitudinal emittance. Kim [ibid] details the mechanics of this process, but the result is an expression for the emittance as a function of the particle phase, as shown in Equation 18.

$$(18) \quad \epsilon_z^{rf} = \frac{1}{nk} (\gamma_f - 1) \sqrt{\sum_n (\Delta\phi_i)^4 \sum_n (\Delta\phi_i)^2}$$

Here γ_f represents the average energy at the exit of the cavity, k is the wave number, and $\Delta\phi$ is the deviation in the particle phase from the average. For a Gaussian distribution, this can be characterized using the standard deviation notation, which yields a slightly simpler expression for Equation 18.

$$(19) \quad \epsilon_z^{rf} = \sqrt{3}(\gamma_f - 1)k^2\sigma_z^3$$

This gives a nice concise expression from which to estimate the effects on the longitudinal emittance caused by the acceleration process and the finite bunch length.

2.3.1.2 RF effects on the transverse emittance

In order to analyze the effects of the RF field on the beam in the transverse coordinates, Kim makes some assumptions about the field profile. This enables some fairly straightforward analysis to be done on the emittance equation. First it is assumed that the longitudinal electric field varies only in z and t , i.e. it is invariant in the transverse direction. Recall the electric field in a pillbox cavity, which follows the zeroth-order Bessel function in the transverse direction. Near the center of the accelerator, where the beam propagates, the small argument approximation of the Bessel function can be used, making Kim's approximation a valid one. Maxwell's equations for the transverse fields then become

(20a)

$$E_r = -\frac{r}{2} \frac{\partial}{\partial z} E_z$$

(20b)

$$B_\theta = \frac{r}{2c^2} \frac{\partial}{\partial t} E_z$$

The transverse fields, which can impart a transverse force on the beam, are then only dependent on the longitudinal electric field. Recall that Equation 10 gives the longitudinal electric field for a pi-mode cavity. In this analysis, an envelope function $E(z)$, is introduced, allowing for an additional spatial variation to Equation 10. Equation 21 expresses the new field.

(21)

$$E_z = E(z) \cos kz \sin(\omega t + \phi_0)$$

By substituting Equation 21 into Equations 20a and 20b, and then into the Lorentz force equation, the transverse momentum imparted onto the beam due to the RF field can be calculated. Here it is convenient to define the envelope function as a Heaviside function that has a value of E_0 in the cavity and zero outside the cavity. This allows one to model the beam behavior during the transition between a spatially varying field and the zero field region of the

transport line beam-pipe. It turns out that by doing this the only component of the transverse Lorentz force that is nonzero and is due to these fields occurs at the exit of the cavity. This can be used in conjunction with the transverse emittance equation defined earlier (Equation 14) to determine the transverse emittance introduced by the beam transitioning from the cavity to the beam-pipe. Kim covers this analysis in detail through the introduction of perturbations in the phase from the average, and then subsequently simplifying. This yields the result in Equation 22, which is the expression for the growth of the transverse emittance due to RF effects, given in terms of the average phase and the phase deviation

(22)

$$\epsilon_x^{rf} = \frac{\alpha k}{n^2} \sum_n x_i^2 \sqrt{\left[\left(\sum_n \Delta\phi_i^2 \right)^2 - \frac{1}{3} \sum_n \Delta\phi_i^4 \right] \cos\langle\phi\rangle + \frac{1}{4} \left[\sum_n \Delta\phi_i^4 - \left(\sum_n \Delta\phi_i^2 \right)^2 \right] \sin\langle\phi\rangle}$$

Here $\langle\phi\rangle$ represents the average phase of the bunch. Equation 21 has a minimum when the final average phase of the beam is at 90 degrees, in which case it simplifies the expression greatly, giving the result in Equation 23.

(23)

$$\epsilon_x^{rf} = \frac{\alpha k}{2n^2} \sum_n x_i^2 \sqrt{\left[\sum_n \Delta\phi_i^4 - \left(\sum_n \Delta\phi_i^2 \right)^2 \right]}$$

By introducing a small perturbation on the phase we can look at the emittance effects near, but not exactly at, the minimum. This is detailed, along with the analysis of a Gaussian distribution, in Kim [ibid]. The important part, which is evident from Equation 23, is that for some given phase distribution there will be a non-zero addition to the emittance as a result of the

discontinuity of the RF field at the exit of the cavity. Kim also shows that the minimum in the transverse emittance will occur when the following expression is satisfied.

(24)

$$\left(\frac{\pi}{2} - \phi_0\right) \sin \phi_0 = \frac{1}{2\alpha}$$

Equation 24 cannot be solved analytically but it is readily solved numerically. This represents the solution as a function of injection phase. Substituting the field parameters for the CSU accelerator and solving Equation 24 yields the result shown in Figure 7.

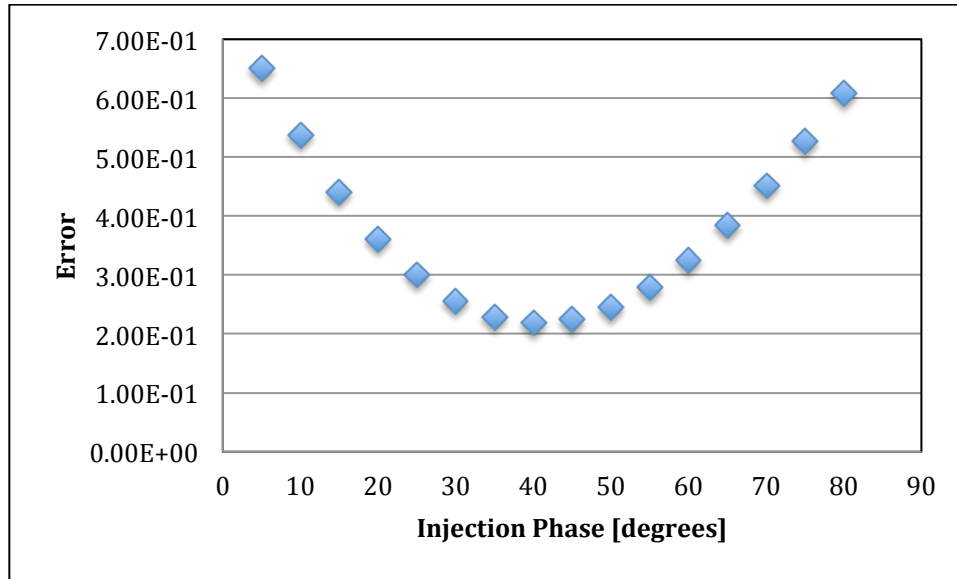


Figure 7: Solution to Equation 24 as a function of Injection Phase. Subtracting the left hand side of Equation 24 from the right hand side solves this, and the result is plotted as a function of the injection phase. The emittance is minimized when this value is zero, or minimum in this case.

Here there is a clear minimum at about 40 degrees, thus indicating that the transverse emittance should be minimized for an injection phase of 40 degrees.

2.3.2 Space charge effects on emittance

Up to this point the discussion has only been concerned with the interaction of a particle beam and the external fields. Due to the nature of the electron beam being a collection of charged

particles occupying a small space, it is necessary to also consider how the internal or self-fields impact the beam quality. Kim's paper goes through great detail in deriving analytical expressions to represent how both Gaussian and top-hat distributions impact the beam emittance. Here the simplest system to analyze is that of a DC beam with a radius of R and a uniform transverse charge density. The electromagnetic field seen by a test particle some distance from the axis of a DC beam, but within the charge distribution, is described by Equations 25a and 25b.

(25a)

$$E_r = \frac{Ir}{2v\pi\epsilon_0 R^2}$$

(25b)

$$B_\theta = \frac{\mu_0 Ir}{2\pi R^2}$$

Here I is the beam current, v is the beam velocity, R is the beam radius, and r is the distance from the beam center. By substituting these terms into the expression for the Lorentz force, the radial acceleration of the beam due to space charge forces can be expressed as:

(26)

$$\frac{dv_r}{dt} = \frac{qIr}{2\pi m_0 \epsilon_0 \gamma v R^2} (1 - \beta^2)$$

As the beam accelerates, β approaches 1 and γ increases without bound. In the context of Equation 26, as the beam accelerates to high energy, the radial acceleration of the beam due to space charge will decrease. This fact allows for the neglecting of space charge forces in high-energy beams. In the CSU accelerator these forces are not negligible and must be accounted for in the dynamics simulations. The results of Kim's analysis of the space-charge forces for different beam distributions yields equations which indicate scaling laws for the space charge

forces and geometric factors that depend on the beam distribution. The most important result of this analysis is shown in Equation 27.

(27)

$$\epsilon_{z,x}^{sc} = \frac{\pi}{4} \frac{1}{\alpha k \sin \phi_0} \frac{1}{I_a} \frac{I}{I_a} \mu_{x,z} (A)$$

Here α , k and ϕ_0 are as defined before. I is the peak current, I_a is 17,000A, and $\mu_{x,z}(A)$ are the longitudinal and transverse space charge factors, calculated based on a chosen beam geometry. Equation 27 is a direct result of analyzing space charge forces in conjunction with the definitions for emittance (Equations 13 and 14), this is provided in detail by Kim.

Compensation for RF-induced emittance is fairly straightforward. Shorter bunches at a particular phase will minimize the impact of the RF fields on the emittance equation. However, space charge forces are a bit different. In beams such as heavy ion beams, having oppositely charged particles co-propagating with the beam leverages a technique called space-charge neutralization. This technique reduces the net space-charge field to minimize the impact of space-charge on emittance. With electron beams, however, it is much simpler to accelerate the beam quickly and leave the space-charge dominated regime. Solenoid fields are then used to compensate for the effect of the space-charge forces. The solenoid field provides a net radial focusing of the beam using both the longitudinal magnetic field and the radial magnetic fields in the fringe region. As the beam propagates through the fringe field region, the radially directed field imparts a transverse kick to the particles proportional to their distance from the axis. When the beam is in the primarily longitudinally directed field region, $v \times B$ has an inwardly directed component due to the transverse velocity imparted to the particles. At the exit of the solenoid, the oppositely directed radial fringe fields remove the rotational-like motion, but since the particles

have moved inward the kick is not as large and so a net radial focusing of the beam is achieved.. This net focusing can be set to compensate for the outwardly directed space charge forces. Interestingly, it is the space-charge forces that compensate themselves, while the solenoid merely acts to place the beam distribution phase space into an orientation that allows this to happen. During this process the beam is accelerated out of the region where space charge is highly relevant. Carlsten [5] provides a more detailed analysis of this elegant method of space-charge compensation in electron guns.

2.4 Beam transport and matching

The beam transport system is used to focus the beam and match envelope functions, $\alpha(z)$ and $\beta(z)$, to the undulator. In order to understand how this is accomplished, one must first look at how a nominal beam transport system would function. This begins with an explanation of the beam trajectory equations.

For an electron beam there is a distribution of the particles in 6D phase space. As discussed earlier, this distribution includes particles with a nonzero angular divergence. It is therefore necessary to periodically focus the particles back towards the ideal trajectory. This is accomplished using either electric or magnetic fields; however, for relativistic particles the electric fields needed are simply beyond the technical limits, while the corresponding magnetic fields required are fairly straightforward to produce. Assuming a vertical field (y-direction) that is allowed to vary horizontally (x-direction), the field can be expanded as:

(28)

$$B_y(x) = B_{y0} + \frac{dB_y}{dx}x + \frac{1}{2!} \frac{d^2B_y}{dx^2}x^2 + \frac{1}{3!} \frac{d^3B_y}{dx^3}x^3 + \dots$$

The constant term will bend the particle trajectories by some amount proportional to the B field and the energy. The linear term has a position dependent field, where particles further from the ideal trajectory see a larger field thus focusing or defocusing the beam, depending on sign. The higher order terms are used to either correct for higher order issues in the beam, or are present due to field errors in the magnets. For the CSU accelerator design, only the first two terms in the expansion are used. Normalizing both sides of Equation 28 to the momentum and multiplying both sides by the fundamental unit of charge gives [1,2]:

(29)

$$\frac{e}{p} B_y(x) = \frac{1}{R} + kx$$

Table 1: Definition of first two magnetic field components in the multi-pole expansion

	Definition	Beam Effect
Dipole Field	$\frac{1}{R} = \frac{e}{p} B_{y0}$	Beam Steering of radius R
Quadrupole Field	$k = \frac{e}{p} \frac{dB_y}{dx}$	Beam Focusing/Defocusing

A dipole is used at the end of the CSU accelerator beam-line to analyze the beam energy spectrum. This will be discussed in Chapter 6. Small dipoles are also used to ensure the beam is indeed centered on axis, but they are not intimate to the beam transport and matching to the undulator, and consequently their effects are not studied here. Quadrupoles, on the other hand, are much more important to the beam transport, as they can manipulate the envelope parameters of the beam for matching to the undulator. Taking the field equation for a quadrupole above and substituting into the Lorentz force equation gives the trajectory equation for a particle in the presence of the quadrupole field

(30)

$$x''(z) - kx(z) = 0$$

Here k is the quadrupole constant and x is the horizontal displacement as a function of position along the accelerator. This is a linear second order ODE that can be easily solved to give the equations of motion for the particle. These equations, given by 31a and 31b, define the phase space evolution of a particle through the quadrupole of strength k .

(31a)

$$x(z) = x_0 \cosh \sqrt{k} z + \frac{x'_0}{\sqrt{k}} \sinh \sqrt{k} z$$

(31b)

$$x'(z) = x_0 \sqrt{k} \sinh \sqrt{k} z + x'_0 \cosh \sqrt{k} z$$

These equations are true without loss of generality for any value k : i.e. for a negative k the hyperbolic sine and cosine functions become sine and cosine functions. For the three cases, $k < 0$, $k = 0$, and $k > 0$ the transport equations represent a focusing quadrupole, a drift space, and a defocusing quadrupole respectively. These equations can then be used to define a system of beam transport elements through the use of transfer matrices. Similar to light optics, the transfer matrices are defined for each beam-line component. In a system of quadrupoles with drift spaces in between this is fairly straightforward. Transport matrices are important to lattice design; however, up to this point these equations have only been discussed in the context of single particles. It is necessary to match the beam parameters given by the phase-space ellipse described in Section 2.2.2 to the undulator, and in order to explain how this can be done, Equations 31a and 31b must take a more general form. First one must note that k is a function of longitudinal position $k(z)$. Assuming a new trial solution that allows for an arbitrary envelope function and phase advance term, both of which are z -dependent, one can come up with the following expression:

(32)

$$x(z) = Au(z) \cos(\Psi(z) + \phi)$$

Equation 30 can be re solved yielding the equations of motion, which describe the beam envelope in phase space as a function of position along the lattice in terms of the phase space coordinates [1].

$$(33a) \quad x(z) = \sqrt{\epsilon} \sqrt{\beta(z)} \cos(\Psi(z) + \phi)$$

$$(33b) \quad x'(z) = -\frac{\sqrt{\epsilon}}{\sqrt{\beta(z)}} [\alpha(z) \cos(\Psi(z) + \phi) + \sin(\Psi(z) + \phi)]$$

Here $\beta(z)$ is the envelope function of the beam, $\alpha(z) = -\beta(z)'/2$, and ϵ is the emittance. These functions correspond to the phase ellipse parameters introduced in Section 2.2.2. This still gives equations in terms of single particles. In order to study how the distribution evolves a further transformation is needed. These transformations are covered in detail in accelerator physics texts, but the important relationship that results from the analysis is:

$$(34) \quad \gamma(z)x^2(z) + 2\alpha(z)x(z)x'(z) + \beta(z)x'^2(z) = \epsilon$$

This relates the Twiss parameters, the single particle equations of motion, and the emittance. Because the emittance is a conserved quantity, this equation can be used to derive propagation matrices for the twiss parameters in a lattice. The general transport matrix for a particle in 2-D phase space is given by:

$$(35) \quad \begin{pmatrix} x_1 \\ x'_1 \end{pmatrix} = \begin{pmatrix} m_{11} & m_{12} \\ m_{21} & m_{22} \end{pmatrix} \begin{pmatrix} x_0 \\ x'_0 \end{pmatrix}$$

For the quadrupole fields this can easily be written in terms of Equations 31a and 31b. Equation 33 used in conjunction with equation 35 creates a transport matrix that propagates the Twiss parameters.

$$(36) \quad \begin{pmatrix} \beta \\ \alpha \\ \gamma \end{pmatrix} = \begin{pmatrix} m_{11}^2 & -2m_{11}m_{12} & m_{12}^2 \\ -m_{11}m_{21} & m_{11}m_{22} + m_{12}m_{21} & -m_{22}m_{12} \\ m_{21}^2 & -2m_{22}m_{21} & m_{22}^2 \end{pmatrix} \begin{pmatrix} \beta_0 \\ \alpha_0 \\ \gamma_0 \end{pmatrix}$$

Here the matrix elements are represented in terms of the general matrix elements in equation 34. This shows how the three Twiss parameters, which represent the beam envelope, are propagated through some arbitrary lattice. As γ is a function of both α and β , a lattice with two quadrupoles can in theory produce any desired output Twiss parameters in a single plane. In reality, however, there are some practical limitations to this. A beam-line with four quadrupoles should be able to achieve the desired output parameters in both the x and y planes. We have chosen to use five quadrupoles to provide us with some additional flexibility in the matching.

3. Electromagnetic Modeling of the Colorado State University Linear Accelerator

The first step in building a full system model of the CSU accelerator and beam-line is to characterize the essential linear accelerator components without the added complication of a particle beam. The process of modeling the accelerating structure and solenoid fields is necessary to produce accurate field maps used in the beam simulations. During this chapter the coupled cavity linac is modeled using a finite-element method code; the solenoid and bucking-coil assembly are similarly modeled. Initial measurements of the linear accelerator are made and compared to the model. In order to insure an accurate model the overall geometry must be understood including the complexities of the geometry, and whether these complexities can be simplified but still produce accurate field maps.

3.1 The Colorado State University linear accelerator

The University of Twente has generously donated the accelerator system currently being reassembled at Colorado State University. The linear accelerator is an 11-cell, coupled-cavity linac operating at 1.3 GHz in the $\pi/2$ mode, with a focusing solenoid and bucking coil assembly used for beam focusing and emittance compensation control. The structure was designed by Los Alamos National Laboratory (LANL) and optimized to produce high-quality beams. Electron bunches generated in the first half-cell are accelerated quickly to leave the space-charge dominated regime and reach a final energy of 6 MeV at the exit of the structure.

The solenoid and bucking-coil assembly provide the necessary focusing to compensate for space-charge effects in the first two cells where the beam is still transitioning to being moderately

relativistic. Figure 8 shows a cross section of the injector system with the critical components highlighted.

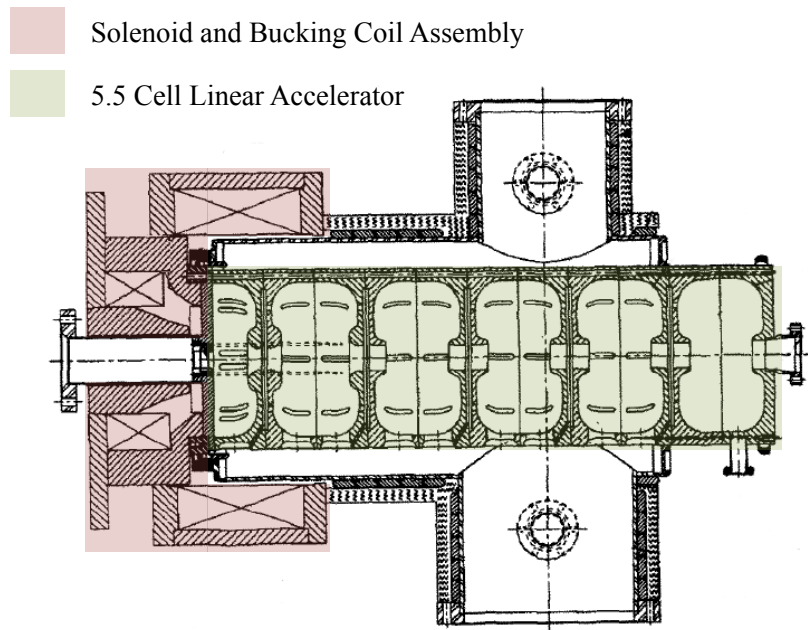


Figure 8: Cross section view of the photo-injector system. Highlighted in red is the solenoid assembly and in green is the linear accelerator.

The modeling of the photo-injector system is broken down into two major pieces, the RF linear accelerator and the focusing solenoid assembly. Development of these models is discussed in that order.

3.2 Modeling of the RF linear accelerator

Modeling of the linear accelerator (green part in Figure 8) utilizes the Los Alamos developed code SUPERFISH [8]. SUPERFISH is a commonly used cavity design tool that employs the finite-element method to solve Maxwell's equations in the frequency domain and subsequently

calculate resonant frequencies and field maps for a provided geometry. The code begins by generating a calculation mesh based on the geometry obtained from user entered coordinates and then, by minimizing an appropriate error function, determines the field geometry of the cavity resonance nearest to a user defined starting point. Depending on the type of problem, the user can specify either axial symmetry or a purely 2D problem.

Many problems in accelerators utilize pure axial symmetry; however, advances in both modeling technology and in cavity design technology have begun to introduce asymmetric properties that produce higher quality devices. Consequently, these more modern structures cannot be fully modeled in SUPERFISH. An important step is to identify the components that are not fully axial symmetric and determine if a reasonably accurate structure model can be made by excluding these elements.

The CSU Linear accelerator has a few of these asymmetries. One very important asymmetry is the coupling slots that allow power to be transferred along the structure. These slots electrically connect the accelerating cavities with the coupling cavities. Figure 9 is a schematic of these coupling slots. While there is symmetry of these slots about the axis, they do not possess full axial symmetry and thus cannot be modeled in SUPERFISH. It is important to note here that the coupling slots are rotated 90 degrees relative to the previous cell along the structure. This is done in order to help minimize the summing of a net quadrupolar field term along the length of the structure, while still allowing for good power flow between the cavities. Other cavity asymmetries are the vacuum ports and input/output couplers. Figure 10 shows a detailed view of the coupling ports and the vacuum ports.

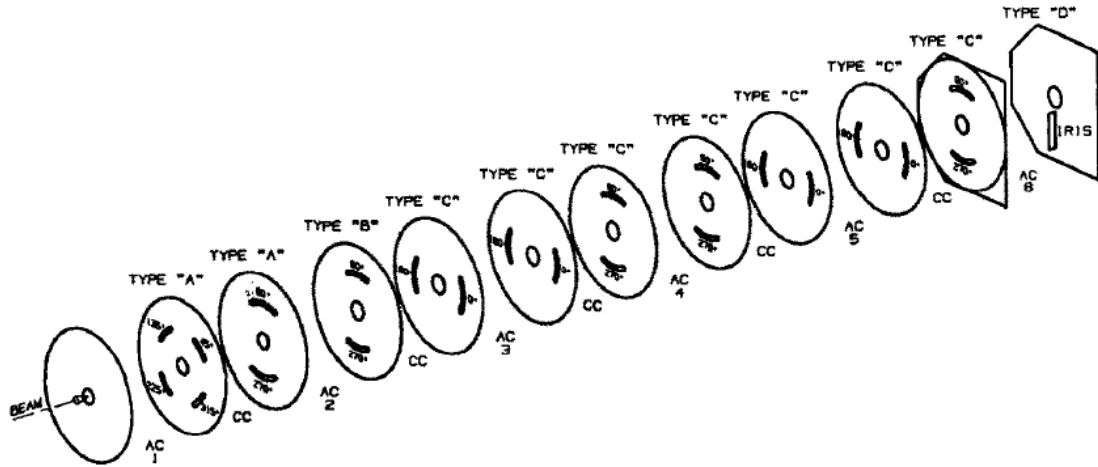


Figure 9: Schematic of the coupling slots in the linear accelerator. A “CC” label between the disks denotes the location of a coupling cell and the location of the accelerating cells are denoted by an "AC" label.

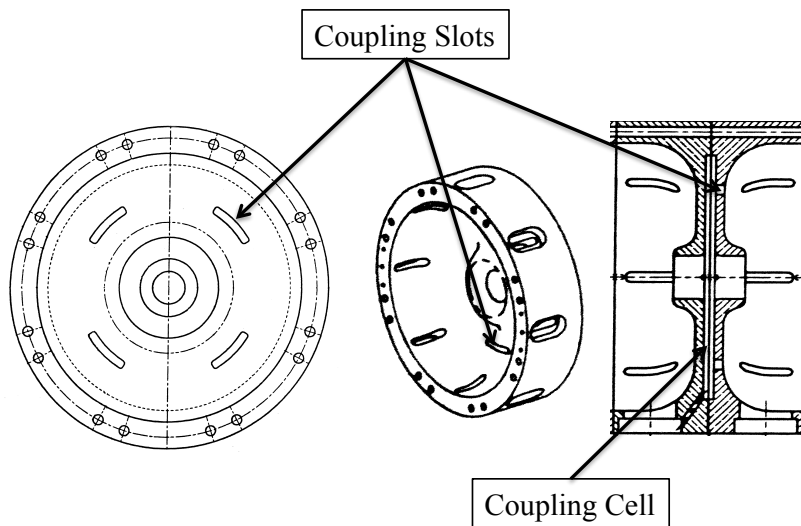


Figure 10: View of details not modeled during this characterization. Note that the other ports visible in the diagram represent vacuum pump-out ports. These are not necessary to model as they have minimal impact on the electromagnetic properties of the structure.

Since SUPERFISH cannot model the coupling slots there will not be adequate power transfer between the simulated cavities if the structure is modeled as a whole unit. The coupling slots, and the coupling cells only really provide energy transfer, as such they are excluded from our initial model. This leaves a 5.5-cell structure that is divided into three cell types, each modeled independently. Once the individual models are complete, the field maps are combined to

generate the field map for the full structure. This is what is used in the beam simulations. The three cell types that need modeling are presented in Figure 11.

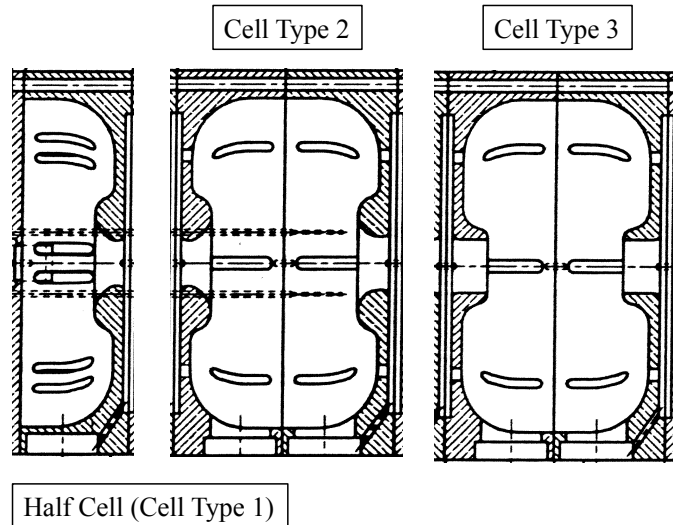


Figure 11: Detailed view of the three cavity cell types modeled during the LINAC system characterization

When modeling each cell type a smooth boundary is used over which the internal fields are solved, i.e. we do not include the vacuum slots and the coupling cells/slots in the simulation.

During the modeling process accuracy is important and the mesh interval is a primary determination of this accuracy. Initially the mesh size is set to a value just small enough to resolve the geometry. The mesh is then systematically reduced until the simulation result (frequency in this case) no longer changes. This process was done for the first half-cell to understand how the mesh interval impacts the simulation result. Figure 12 shows the resonant frequency of cell 1 as a function of the mesh interval. This shows a good convergence of the solution for a mesh interval around 0.01 cm.

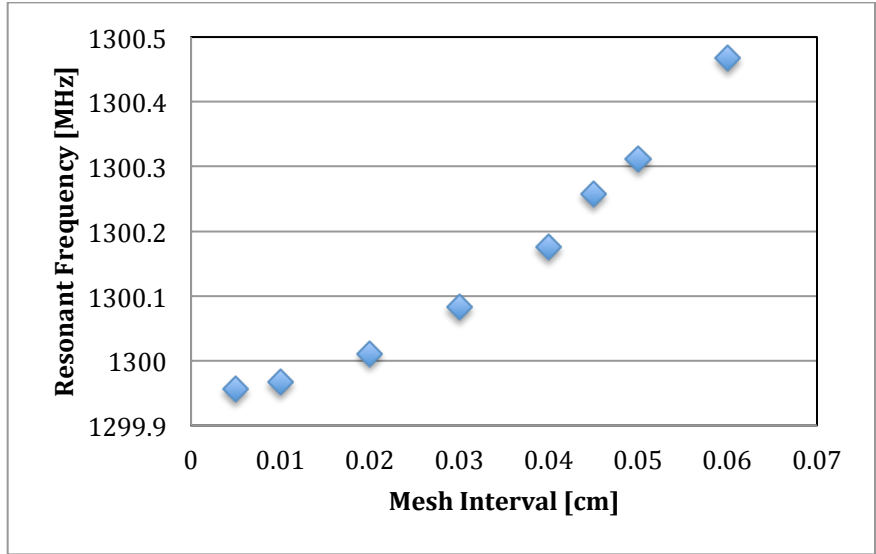


Figure 12: Resonant frequency as a function of the mesh interval showing relative stability. Note that above a mesh interval of 0.06 the mesh was too coarse for SUPERFISH to provide a satisfactory solution.

High accuracy in the resonant frequency is, however, not critical because during the beam simulations, field maps provide spatial field profiles that are driven with a sinusoidal component in time by a user-defined frequency. In other words, the user tells the simulation code what frequency to use to drive these fields maps. However, it is important to understand how the mesh impacts the model accuracy and to be close (within 100khz or so) to the resonant frequency, the result of which was shown in figure 12.

With an understanding of how these cells are modeled, what mesh size is needed for the desired level of accuracy, and what items are excluded, each cell is then modeled individually using SUPERFISH and it's respective field map produced. Figure 13 shows the model and field map for the first cell type. The field map from the first half-cell is optimized to have a high flatness spatially. This helps to reduce nonlinearities that can occur from the interaction of the fields with the beam as it is created.

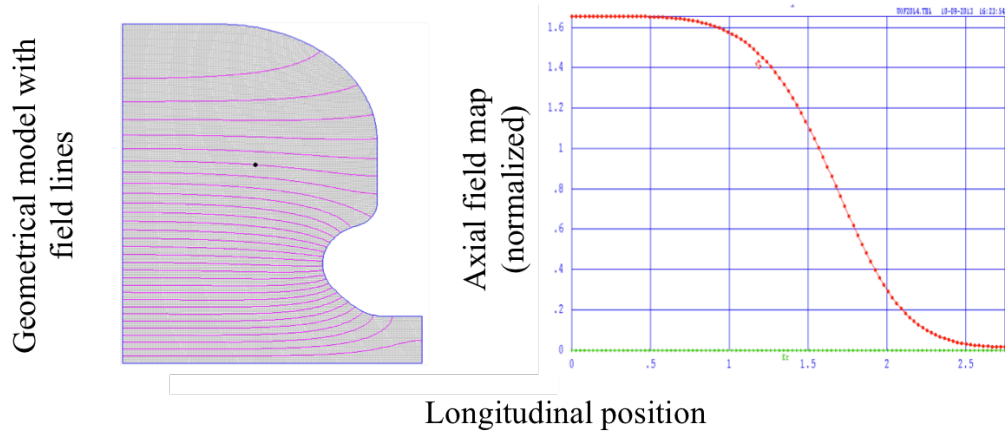


Figure 13: Cell type 1 geometry and field contour model with axial field map on the right. The simulation file used to produce this model is provided in Appendix A.1

As the cavity is modeled separately from the whole geometry, the field goes to zero at the boundary. The peak field in this cell is high to accelerate the beam quickly out of the space charge dominated regime.

The next cell modeled along the structure is the type 2 cell. Figure 14 shows the field map and geometrical boundary for this cell type.

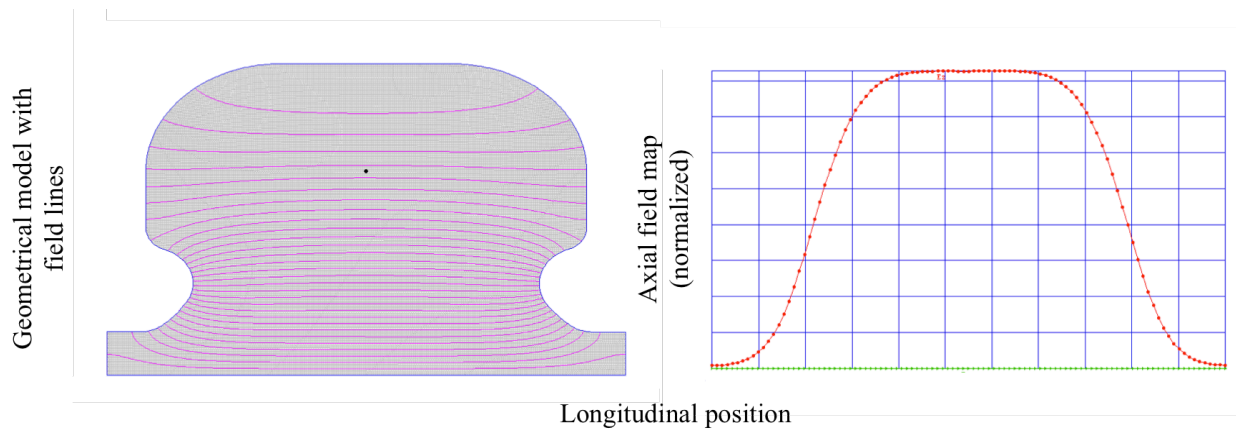


Figure 14: Cell type 2 geometry and field contour model with axial field map on the right. The simulation file used to produce this model is provided in Appendix A.2

Similar to the first cell, the second cell is also optimized for high field flatness. This results in a less efficient energy transfer to the beam but the fields in this structure are higher as a result.

The final type of cell modeled is slightly different than the previous two cells and is optimized to have an efficient net transfer of the field energy to the beam energy. The field map and geometry profile of this cell is shown in Figure 15

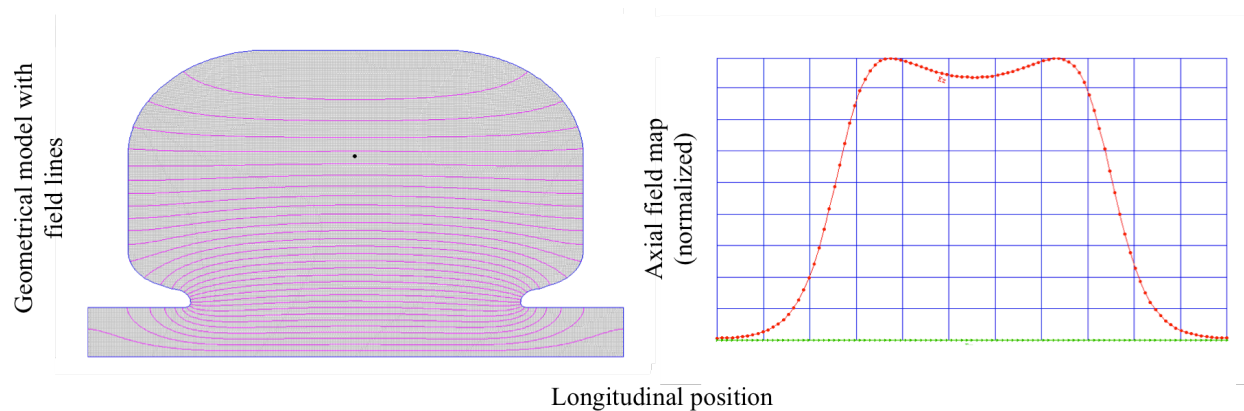


Figure 15: Cell type 3 geometry and field contour model with axial field map shown on the right. The simulation file used to produce this model are given in Appendix A.3

The field map has some bumps in the longitudinal profile that are caused by the “nose”; however, due to the beam being moderately relativistic at this point along the cavity, these spatial variations do not impact the bunch dynamics as harshly. It is more important in this section of the LINAC to maximize the energy transfer efficiency. By adding the nose cones the effective shunt impedance is higher and consequently the energy transfer has greater efficiency.

The shunt impedance and quality factor data were computed using SUPERFISH. These values are presented in table 3.1. It should be noted that these do not represent the structure quality factor and the structure shunt impedance but are merely guides to verify that the linac basic characteristic are understood.

Table 2: Quality factor and shunt impedance data computed for the three cell types by SUPERFISH. Shunt impedance data are for individual cells

Cell Type	Quality Factor	Shunt Impedance [M Ohms/m]
Type 1	25738	86.0012
Type 2	25745	86.0291
Type 3	26369	96.383

This shows that indeed the shunt impedance is higher for the cell type 3. Additionally, cell type 3 has a higher quality factor thus further showing that it will maximize the ability to transfer energy from the rf power to the cavity fields.

Combining the individual field maps and normalizing them to the appropriate peak fields obtained from the University of Twente produces the field map for the whole structure. A previous field map from Los Alamos National Lab [9] was compared to the field map generated by stitching the cells together and is shown in figure 16. Qualitatively this shows that the cavity field model generated is accurate for use in beam simulations to characterize the system.

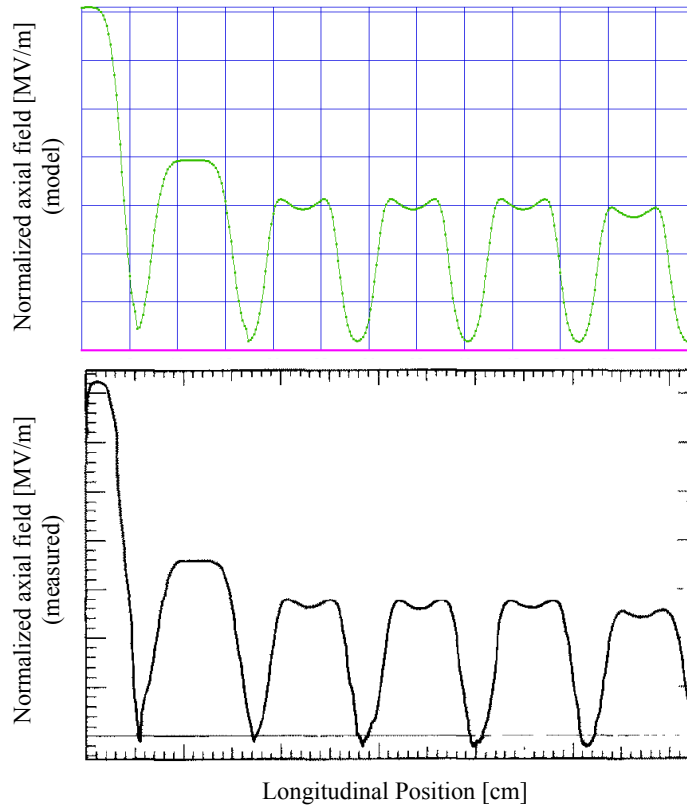


Figure 16: Comparison of the axial field map modeled with SUPERFISH to the data from previous work [9]

3.3 The solenoid and bucking coil assembly

As discussed in the previous chapter, the solenoid is a critical piece of the puzzle because of its ability to control the space-charge effects, and focus the beam during initial acceleration. Using the drawings from the University of Twente a geometrical model of the assembly was created; this geometry is shown in Figure 17.

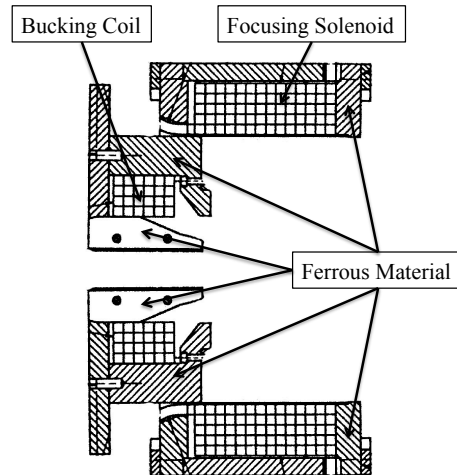


Figure 17: Solenoid assembly drawing highlighting the important ferrous material and the two coils

SUPERFISH comes with another field solver called PANDIRA [8] that is used to model the solenoid and bucking coil assembly. PANDIRA is a 2D static field solver that computes magnetic fields or electric fields, depending on what is desired. Similar to SUPERFISH, PANDIRA is axially symmetric. The code models ferrous material through the use of a linear permeability model which by definition does not account for any magnetic hysteresis or saturation effects. Current distributions are used in the place of wires to model the two coils.

The solenoid assembly is modeled in four different regions. These regions consist of the solenoid and bucking coil themselves, shown in figure 17, and their subsequent surrounding magnetic material. In order to prepare the solenoid and bucking coil model for use in the beam dynamics simulations it must first be tuned to have zero field on the cathode. This is essential to ensure that the particles do not have any additional azimuthal velocity (i.e. the fields are not adding to the any preexisting azimuthal velocity present from emission) from the radial and longitudinal magnetic fields. Additional components to the beam motion have an impact on how the beam propagates through the system and can have adverse effects on the beam dynamics.

Since the solenoid and bucking coil are an assembly that fits onto the LINAC cavity we know physically where the zero field region should be. To make sure this region has a magnetic field of zero, the simulation is run with zero excitation in the solenoid but with some nonzero, known excitation, in the bucking coil. This produces some known field on the cathode per unit excitation in the bucking coil. This process is repeated with the solenoid turned on and the bucking coil turned off. Scaling the results appropriately one can then ensure a zero field at the cathode over the desired range of correction solenoid strengths. Figure 18 shows the geometry and field map of the assembly and the on-axis axial (red) and radial (green) field profiles normalized to the radius.

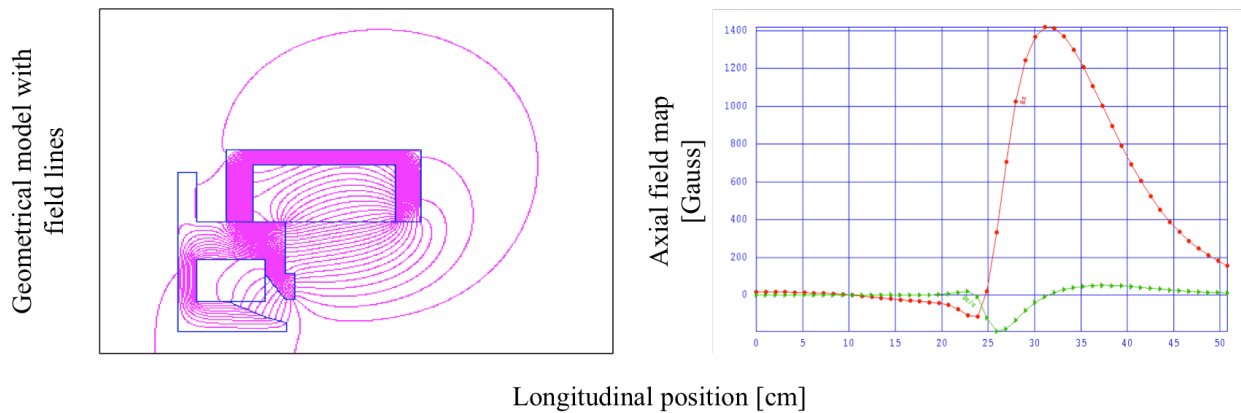


Figure 18: Numerical model of the Solenoid showing the axial field map. This model was produced using PANDIRA. The red line is the longitudinal magnetic field on axis and the green line is the radial magnetic field normalized to the radius or B_r/r . The simulation files used to produce this model are given in Appendix B.

This concludes the section on the electromagnetic models needed to begin beam simulations on the accelerator system. Before beginning the process of simulating the beam, however, some initial measurements of the LINAC were taken in order to partially verify the simulation results.

3.4 LINAC measurements and data analysis

During the initial characterization process it is helpful to gain as much knowledge of the system as possible. As part of this process some initial checkout measurements were made of the structure. The accelerator is currently not exposed to air and it is necessary to keep it as clean as possible, therefore measurements were taken through the RF window thus minimizing the impact on the structure.

The RF window is a ceramic device that is transparent to microwaves and separates the high vacuum from atmospheric pressure. On one side of the window is the high vacuum of the accelerating structure while on the other side is the, perhaps pressurized, rf waveguide. Sulfur hexafluoride gas at some modest pressure is typically used in the waveguides to help prevent electrical breakdown caused by the high powers propagating in the waveguide system.

The network analyzer was attached to an L-band waveguide rf launcher that bolts onto the outside of the RF window allowing measurements to be taken with minimal impact. In this type of configuration only one type of measurement can be taken, the S11 reflection coefficient. The network analyzer is first calibrated, and is then attached to the L-Band RF launcher to generate the S11 spectrum for the device. For characterizing the mode structure it is expected there will be 11 resonances in the S11 curve centered on the 1.3 GHz $\pi/2$ -mode resonance. Figure 19 shows these measurements.

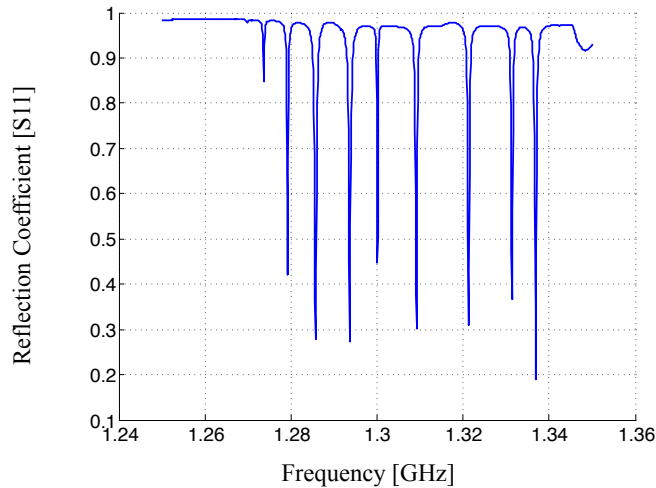


Figure 19: S11 measurement of the RF cavity from 1.25GHz to 1.365GHz. Note that the broad resonance-like signal on the right hand side of the spectrum is an issue with the measurement and not a mode.

As is expected, there are eleven resonances where the reflection coefficient dips below one. This corresponds to the eleven cells in the structure. The first and the last resonances are difficult to see on this plot; however, the detailed view in Figure 20 clearly shows these resonances. Additionally this detailed view provides important information about each resonances' depth and width. This information is used to calculate the quality factor of each mode.

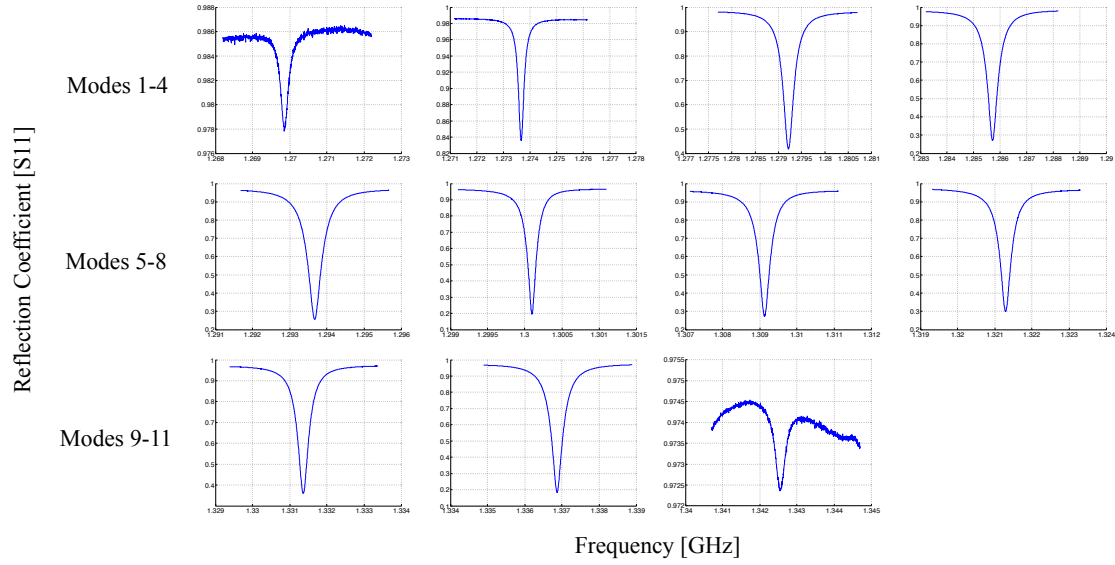


Figure 20: Detailed view of each mode. These data were used to determine the full width half max of the resonance necessary for quality factor calculation

From the data presented in Figure 20 the precise mode location and it's full width half max can be measured. The quality factor in terms of the S11 measurement is defined Equation 37:

(37)

$$Q = \frac{f_{res}}{f_{FWHM}}$$

Where Q , is the quality factor, f_{res} is the resonant frequency of the mode, and f_{FWHM} is the full width half max of the S11 measurement for that mode. Executing this calculation on each of the modes gives their respective quality factors. This result is shown in Figure 21. Previous work published by Los Alamos National Lab on this system measured the cavity Q and a shunt impedance. CSU is not currently equipped to take a shunt impedance measurement for the cavity; however, the quality factor can be compared. This comparison is shown in table 3.

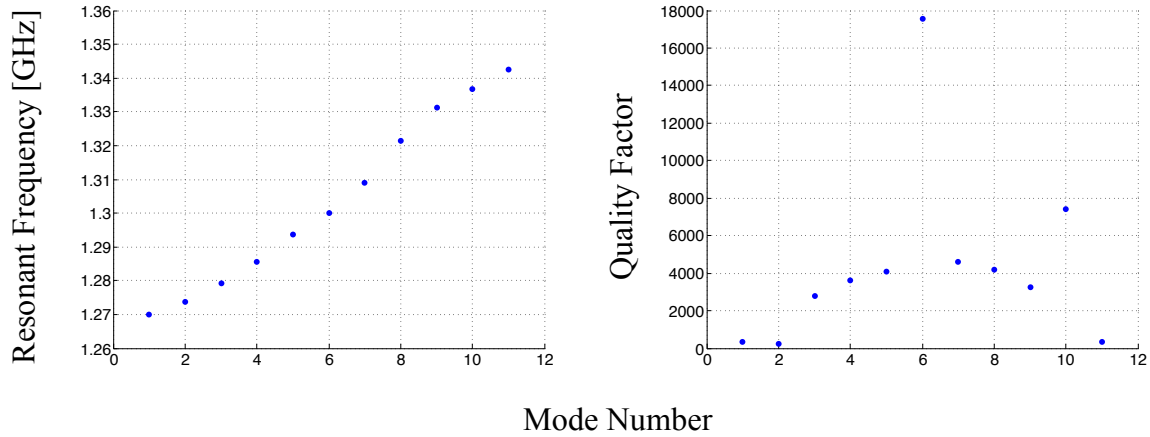


Figure 21: Resonant Frequency and quality factor as a function of the mode numbers. Mode numbers are in order of appearance on Figure 18.

Table 3: Los Alamos Measurements vs CSU measurements

	Los Alamos Measurement	CSU Measurement
Quality Factor	16144	17551
Shunt Impedance	53 MOhm/m	(Not Measured)

The full width half max of the 1.3-GHz mode used to compute the quality factor also provides bounds for when the cavity is on or off resonance. Additionally, the mode data can be used to determine the frequency range for maintaining less than a 5% variation in the fields. This corresponds to an 8kHz bandwidth. As power is dissipated into the cavity walls the cell geometry will expand causing a frequency shift. In order to maintain the resonance within the 8kHz band, a cooling system is used to regulate the cavity temperature. Through the use of a linear thermal model on the cell geometries shown in the previous section, the shift in resonance per degree Celsius was calculated to be 20.547 kHz/C. To achieve a field variation less than 5% the temperature of the cavity must be held to within plus or minus 0.19 degrees C of the temperature set point.

Having completed the electromagnetic model of the LINAC and having done some initial measurements, the accelerator system model is ready to add the effects of a beam and then move to the beam-line simulation process.

4. Characterization of the RF Linear Accelerator

With a complete model of the primary accelerator components, the next step is to introduce an electron beam and study the interaction of the beam with the accelerator components. This chapter begins with a description of the simulation code used to model the injector, and a characterization of how the simulation parameters impact the results produced. This is followed by a study of how the adjustable parameters in the gun, in our case RF phase, RF field strength, solenoid strength, beam current, cathode spot size, and bunch length, impact the beam quality. And finally, the details of the initial settings for operation are provided.

4.1 PARMELA beam dynamics calculations and sensitivity analysis

Beam simulations for the injector are performed in PARMELA [10]. PARMELA is a Los Alamos developed single-pass linear accelerator design code. It operates by using field maps obtained from SUPERFISH and PANDIRA to calculate the trajectories for individual particles. PARMELA also has two space-charge routines that compute the interactions of the particle beam's self fields on the distribution. The primary space-charge routine divides the bunch into charge disks based on binning the nearby particles, and by the user specified mesh intervals. Impulses are then applied to the beam trajectories that are taken into account in the dynamics calculation. The other algorithm is a full 3D PIC simulation, this is not used as it has long computation time, and the degree of accuracy is not necessary for initial system characterization.

There are a few parameters that can be varied by the user in order to control the accuracy of the calculation. Typically, increasing the simulation accuracy translates to a longer simulation time; therefore, when running a large number of simulations it is important to be accurate within

acceptable levels while simultaneously not having excessive computation times. The user-defined parameters that have the greatest impact on simulation accuracy are the integration step size, the number of particles in the simulation, and the longitudinal and transverse mesh size of the space-charge routine. The first two are in some ways not dependent on the latter two; however, the inclusion of space charge will impact the simulation. In order to assess what parameters will give a good level of accuracy for our machine, these values were varied and the emittance analyzed to determine the resolution needed.

4.1.1 Sensitivity to number of particles (without space charge)

The first parameter varied was the number of particles in the simulation. This parameter is important to understand because a real beam contains on the order of 10 billion particles thus requiring supercomputers to perform "complete" simulations. Simulation of a beam with this many particles is impractical and for these studies unnecessary. To simplify the calculation the space-charge routine was tuned off, and the integration step was set to 0.1 degrees of RF phase. The number of particles was then scanned between 100 and 10,000 particles. Figure 22 shows the emittance as a function of the number of particles for the described conditions.

While the plots do not show highly smooth curves there is a point, after about 1000 particles, where the emittance is relatively unchanged as the number of particles increases. The transverse emittance is much less well behaved than the longitudinal emittance, however both do reach relatively stable points. It is important to note here that only the x emittance is being shown. The code has axial symmetry, and the field maps are also axially symmetric; therefore, it is not

necessary to show the y emittance. For the duration of this chapter, only the x emittance is shown and is referred to as the transverse emittance.

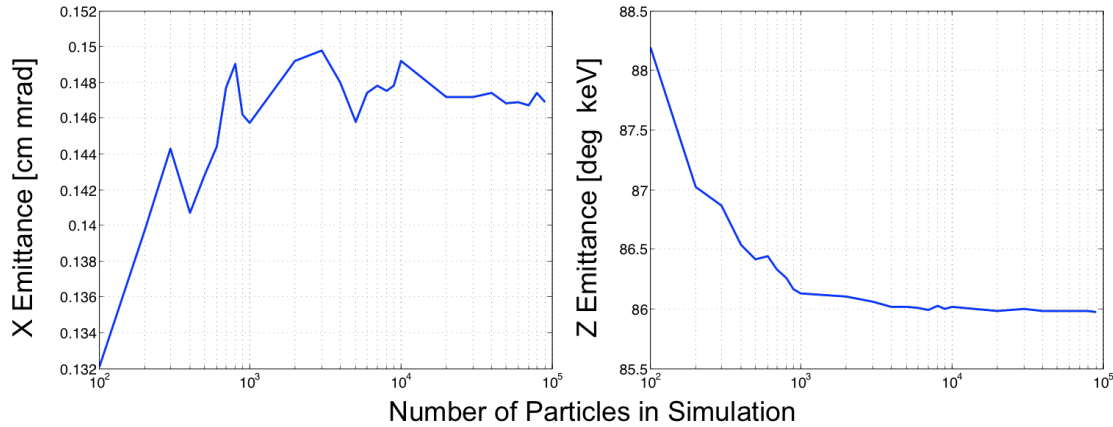


Figure 22: Transverse and Longitudinal emittance as a function of the number of particles plotted on a semi-log scale.

To insure the simulation is well inside the good region for particle number the next series of simulations were run with 5000 particles.

4.1.2 Sensitivity to integration step (without space charge)

The integration step is a phase interval over which PARMELA computes the particle dynamics. The shorter the interval the more accurate the calculation; however, as with the number of particles the shorter the integration step the more calculations must be done and therefore the simulation time will increase. There is a point similar to the number of particles where the decrease in the integration step will not significantly increase the simulation accuracy. Figure 23 shows the transverse and longitudinal emittance as a function of the integration step.

Here it is clear that with integration step sizes of less than 0.1 degrees the calculation does not change significantly. The simulation time for this level of accuracy is a bit long and it may be

possible to compromise on the accuracy and increase the integration step size in order to discover trends rather than provide explicit answers.

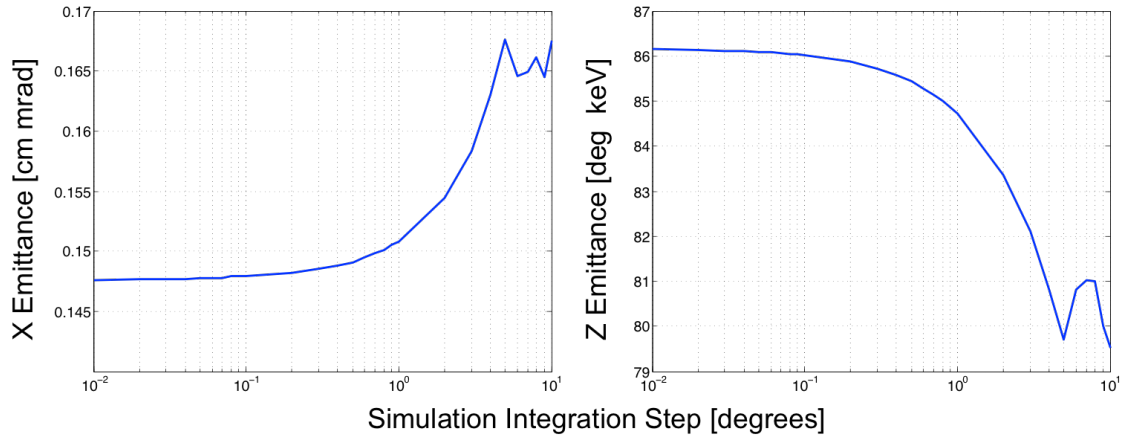


Figure 23: Transverse and longitudinal emittance as a function of the integration step. Convergence is clear after 0.1 degrees

Once trends are identified higher resolution calculations can be done on specific parameters to obtain a better idea of the emittance values.

4.1.3 Sensitivity to space charge routine parameters

The relative amount of space-charge to include is determined by the beam current parameter in the space-charge routine. This is defined by the bunch charge multiplied by the RF frequency. In the case of the CSU accelerator a range of charges can be used for operation between 1 nC and 5 nC. A modest amount of charge, 2.3 nC, was used to characterize the sensitivity of the space-charge parameters. The space-charge routine divides the beam into longitudinal and transverse segments. Then, an impulse force is applied to the beam distribution that can be executed at user specified intervals with respect to the dynamics calculations; for the simulations in this thesis space-charge impulses are calculated at each integration step. The granularity of this calculation will have a significant impact on the emittance. In order to insure sufficient accuracy the emittance is studied as a function of the transverse and longitudinal mesh size of the space-

charge computation. Figure 24 shows both the transverse and longitudinal emittance as a function of the longitudinal mesh number. This corresponds to the number of mesh elements used in the space charge calculation along the length of the beam. Increasing this number means increasing the resolution of the calculation.

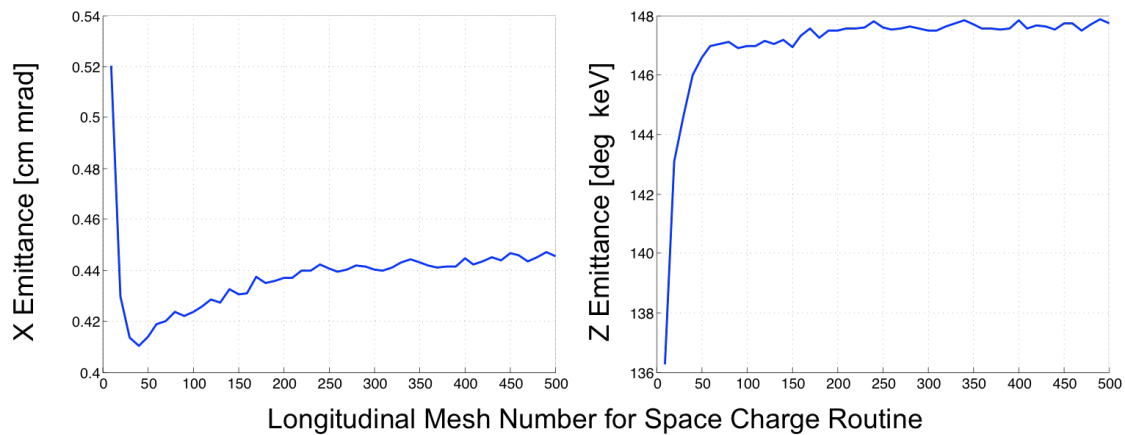


Figure 24: Transverse and longitudinal emittance as a function of the longitudinal mesh number.

While varying the longitudinal mesh number the transverse mesh number was held at 50. It is clearly visible that the longitudinal mesh number effects the emittance in both planes. The stability in the longitudinal emittance calculation comes much faster than the transverse emittance; however, both become relatively stable after a mesh number of 200. Note also that while the transverse emittance takes longer to stabilize, the magnitude of the transverse emittance variation is much smaller compared to the variation in the longitudinal emittance.

Figure 25 shows the variation in the transverse and longitudinal emittance as a function of the transverse mesh number. For these simulations the longitudinal mesh number was held at 200. Here it is clearly visible that the emittance calculation becomes relatively stable after a transverse mesh number of about 50.

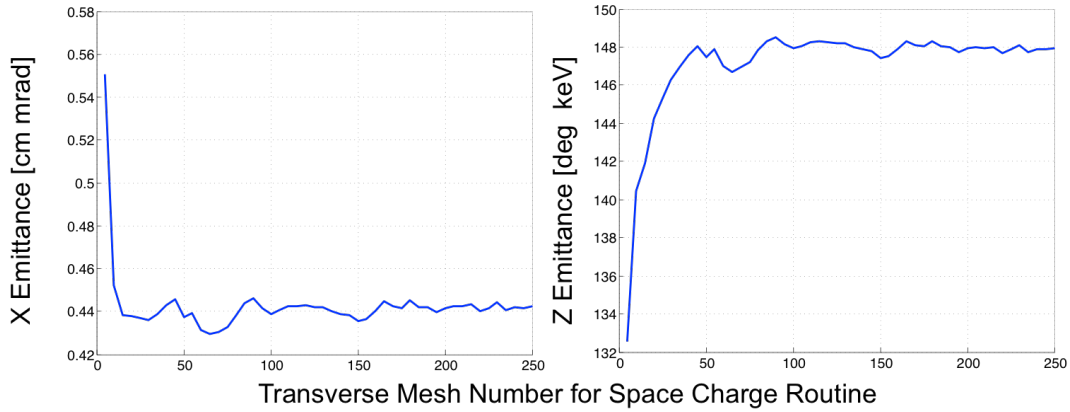


Figure 25: Transverse and longitudinal emittance as a function of the transverse mesh number.

There is still some variation in the emittance in both Figures 24 and 25 that looks like numerical noise; however, this is likely due to the space-charge routine not being a full 3D routine.

4.1.4 Sensitivity to number of particles and phase step with space charge

To address the sensitivity of particle number and integration step with the inclusion of space charge, the space charge mesh was set to 200 and 50 for the longitudinal and transverse mesh numbers respectively. Then, as before, both the integration step and the number of particles were assessed for accuracy of the emittance calculation. Figure 26 shows the emittance as a function of the integration step for a 2.3 nC beam with 5000 particles.

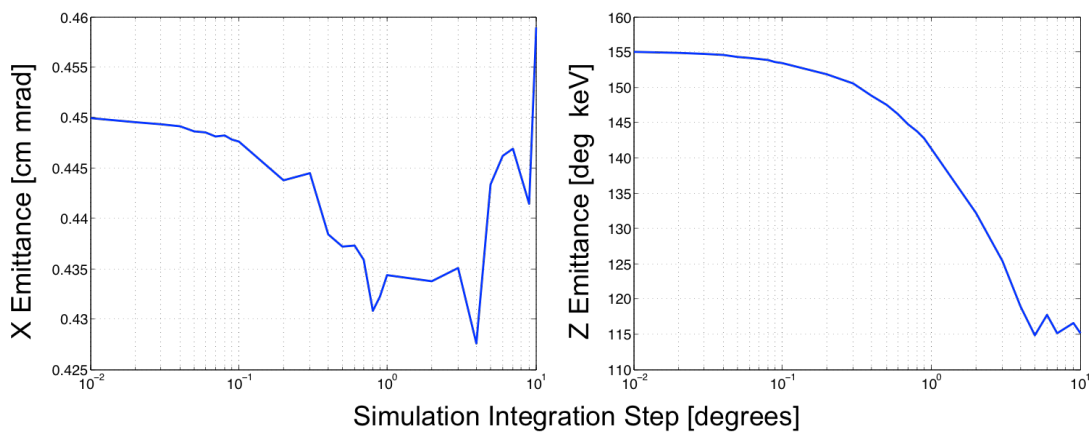


Figure 26: Transverse and longitudinal emittance as a function of the integration step.

Figure 27 shows the emittance as a function of the number of particles for a 2.3 nC beam with an integration step of 0.1 degrees.

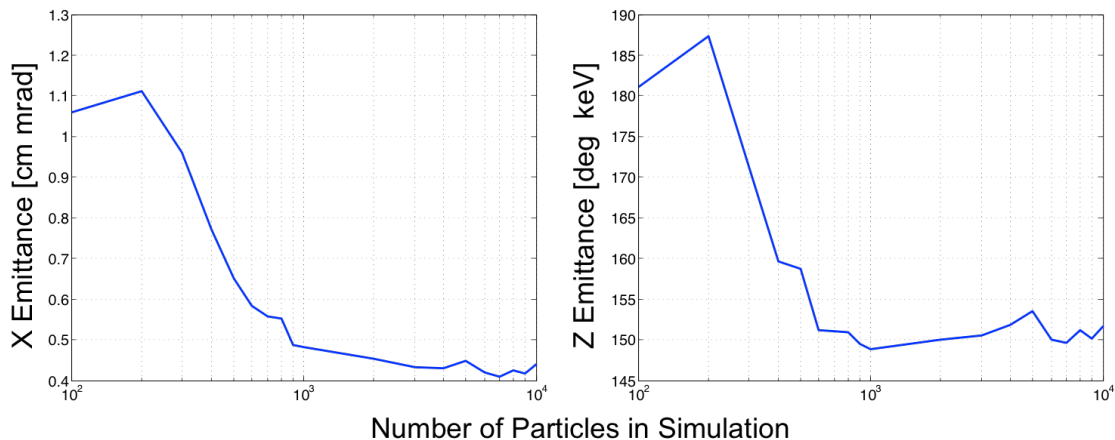


Figure 27: Transverse and longitudinal emittance as a function of the number of particles

Here it is clearly visible that the calculation stabilizes after about 1000 particles. As a summary to this section, simulation parameters that will produce numerically accurate numbers for the CSU accelerator were determined. The space charge intervals should be at least 200 and 50 for the longitudinal and transverse mesh intervals respectively, the integration step should be at or below 0.1 degrees, and the particle number should be at or above 1000 particles. With this knowledge the system parameters, RF phase, beam current, bunch length, cathode spot size, and solenoid strength, can be varied and their effects studied.

4.2 Injector simulation studies

Because the injector is already built, the user has no control over parameters such as the cavity field profiles or the magnetic focusing field profile. The parameters that can be varied however, are the RF phase, the RF field, the solenoid field, the bunch charge, the cathode spot size, and the bunch length. The RF phase is addressed first. This is followed by an analysis of the solenoid

field in tandem with the bunch charge, as these two are highly coupled. Finally the effect of variable cathode spot size, and bunch length are addressed.

4.2.1 RF Phase effects

During the theoretical discussions it was shown that by changing the phase of the beam relative to the RF waveform the beam could experience focusing in either the transverse direction or the longitudinal direction. To study how this manifests itself in the CSU accelerator the phase parameter is scanned while all other parameters are held constant. For these simulations the beam charge was set to 2.3 nC, the solenoid focusing field was 1.4 kGauss, the bunch length was set to 20 degrees (about 40 ps), and the cathode spot size was set to 0.2 cm. The injection phase was then scanned from zero to one hundred eighty degrees.

For a bunch length of 20 degrees it is expected that significant losses will occur below 10 degrees as some particles are injected when the field is negative and therefore cannot propagate. Additionally, for a short gap ($\lambda/10$), a single particle emitted later than 115 degrees does not gain sufficient energy to exit the cavity, and returns to the cathode due to the field changing sign [11]. The first cell of the CSU accelerator is not short, about $\lambda/4$, and additionally the bunch length is relatively long at 20 degrees; therefore, we expect to see significant losses well below 115 degrees relative to the RF. This is evident in the phase scan which showed that only in the range of 10-80 degrees did 100% of the beam make it out of the injector. Both the transverse and longitudinal emittance were studied as a function of injection phase. The variation in the transverse emittance as a function of the RF phase is shown in Figure 28.

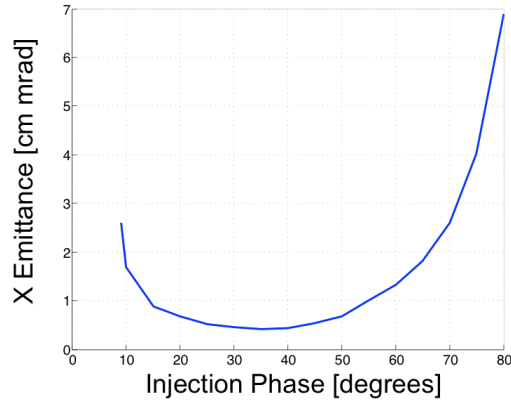


Figure 28: Variation of the transverse emittance as a function of the RF injection phase

In Chapter 2, 40 degrees was shown to satisfy the criteria for minimizing the transverse emittance. Here it is clearly visible that there is a broad minimum in the transverse emittance as a function of injection phase between 30 and 50 degrees, with the optimum value at about 35 degrees.

The variation in the longitudinal emittance was also considered. The discussion in Chapter 2 showed that the longitudinal emittance would be minimum for a particular operating phase, around 10-15 degrees. Figure 29 shows the variation in the longitudinal emittance with RF injection phase.

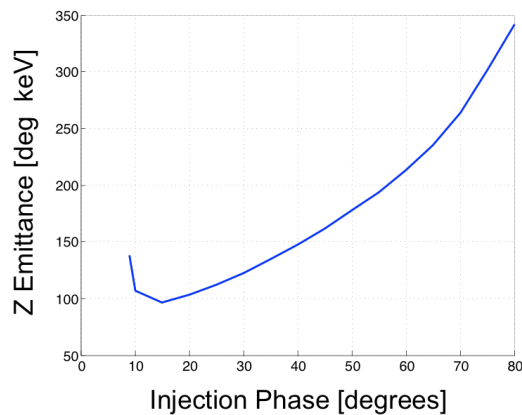


Figure 29: Variation in the longitudinal emittance as a function if the injection phase

Here it is clearly visible that the longitudinal emittance is a minimum at about 15 degrees RF phase. The results of these two scans show that the modeled injector performance as a function of injection phase is consistent with expectations.

4.2.2 Solenoid focusing and beam charge effects on emittance

Space-charge effects in the beam can be compensated for in two primary ways. A solenoid field can be used to compensate for space-charge forces while an increase (or decrease) in the beam charge directly increases or decreases these forces. The bunch length also impacts the space charge forces but this will be addressed separately. To study the impact of the solenoid field and the beam charge, these two parameters are varied and the beam emittance analyzed. During these simulations the injection phase was set to 40 degrees, the bunch length was set to 20 degrees (40 ps), and the cathode spot size was set to 0.2 cm.

To adjust the beam current PARMELA's space charge routine can simply be adjusted to include more or less charge. To adjust the solenoid field a scaling factor is used to either increase or decrease the fields. As discussed in Chapter 3, because the magnetic field model does not include any nonlinear permeability, a linear scale factor will not impact the shape of the field, only the magnitude. At a scale factor of 1 the peak magnetic field is 1420 Gauss. The beam current was varied in 0.4 nC increments from 0.8 nC to 3.2 nC, and the solenoid field was varied from 710 Gauss to 1700 Gauss. The result of these scans are shown in Figure 30. A clear minimum in the transverse emittance as a function of the solenoid strength is visible. Additionally as the beam charge is increased, that minimum emittance shifts towards the right. This corresponds to an increase in the solenoid field. This result is expected as an increase in the beam charge results in a larger space-charge force requiring a larger magnetic field to compensate.

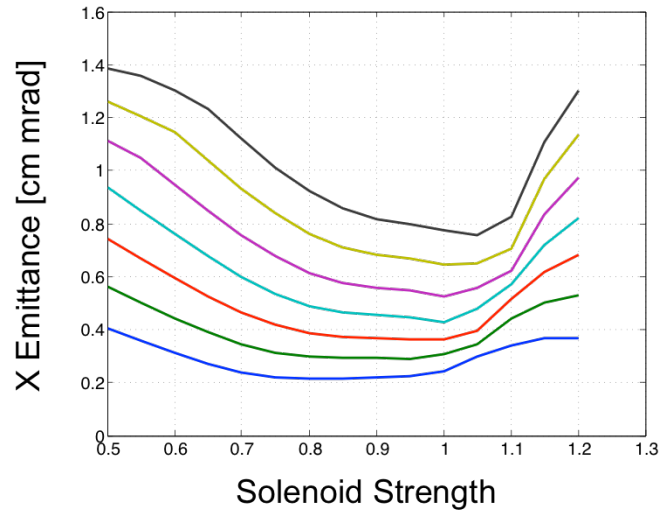


Figure 30: Transverse emittance as a function of the solenoid strength, from bottom to top shows the increase in beam current from 0.8 nC to 3.2 nC in 0.4 nC increments

When operating the machine it is necessary to study how these two parameters are related and to know what field strengths to use for which beam currents. It is important also to understand the direct relationship between the beam charge and the emittance. Figure 31 shows the minimum transverse emittance as a function of beam charge.

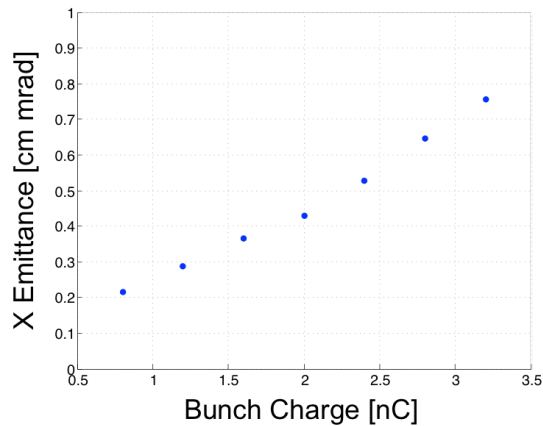


Figure 31: Minimum transverse emittance as a function of the bunch charge.

This shows that as the bunch charge is increased the emittance will increase as well. This is expected and in general there is a fairly well defined scaling between emittance and bunch

charge. The solenoid field also has some effect on the longitudinal emittance, which is expected to be small. Figure 32 shows this relationship.

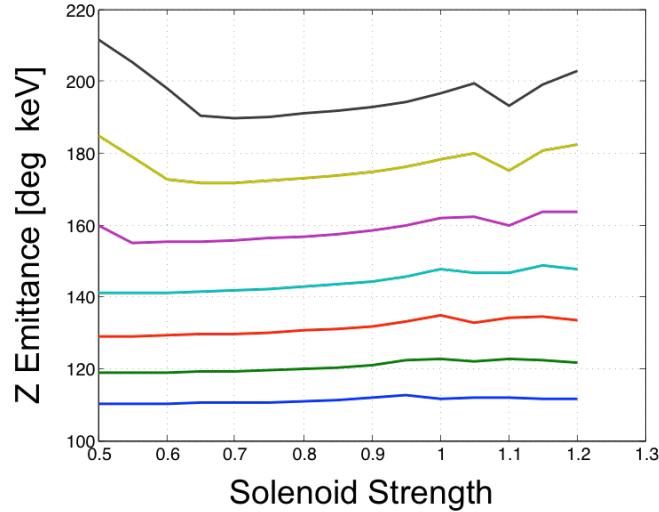


Figure 32: Longitudinal emittance as a function of the solenoid strength. From bottom to top indicates an increase in beam current

Here it can be seen that, in general, there is a fairly weak correlation between the solenoid field and the longitudinal emittance. Because the space-charge force compensated for by the solenoid is a transverse force, it is expected that the correlation between longitudinal emittance and the solenoid field is weak. On the left hand side of the plot there are currents that show a decrease in the emittance as the solenoid field increases. This effect is caused by insufficient focusing in the solenoid resulting in particles being ejected from the simulation region. Additionally, on the right end of the curve there is a dip in the longitudinal emittance as a function of the solenoid strength. This is most pronounced for the higher current cases however this dip exists for all cases. As the scope of this work is to provide an initial system characterization the cause of this phenomena was not investigated further.

4.2.3 Cathode spot size effects on emittance

The cathode spot size is adjusted by changing the maximum radius of the input electron beam. Because the injector utilizes a photocathode drive, this adjustment is the same as increasing the laser pulse spot size. For a very small bunch it is expected that the space charge forces will increase which could have an adverse impact on the emittance. However, as the bunch increases in diameter the overall area in phase space increases, thus increasing the emittance. For a beam charge of 2.3nC, a solenoid strength of 1420 kGauss, an RF injection phase of 40 degrees, and a pulse length of 20 degrees, the bunch radius was scanned between 0.05 cm and 0.5 cm. The transverse emittance as a function of spot size is shown in Figure 33.

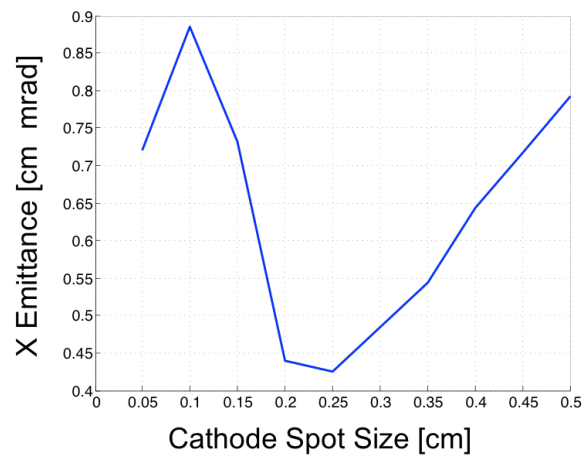


Figure 33: Transverse emittance as a function of the cathode spot size

Here there is a clear minimum in the transverse emittance at about 0.25 cm. As expected the emittance is large for a smaller spot size and again increases as the spot size is increased away from 0.25 cm. The feature on the left side of the plot is caused by space charge expelling particles out of the simulation. Figure 34 shows the variation in the longitudinal emittance as a function of the transverse spot size. Here as the spot size is increased the longitudinal emittance actually decreases. This is because increasing the transverse spot size decreases the space charge forces, which interact both longitudinally and transversally.

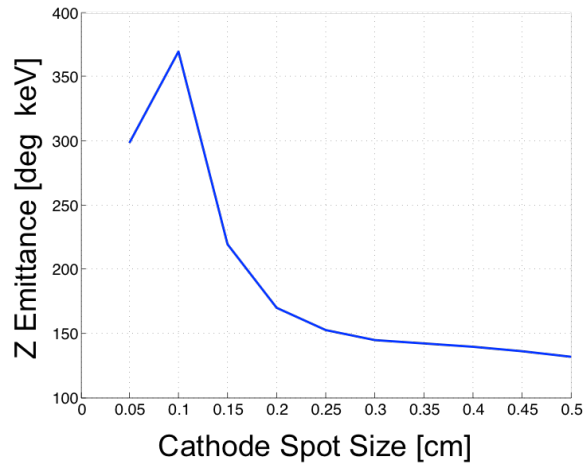


Figure 34: Longitudinal emittance as a function of cathode spot sizes

Unlike the transverse emittance, increasing the transverse spot size does not increase the area in the longitudinal phase space, and there is no corresponding increase of the emittance in this plane.

4.2.4 Bunch length effects on emittance

The bunch length is adjusted by changing the duration of the laser pulse incident on the cathode. To study this effect in simulation, the bunch length can be set directly inside the PARMELA input file. For a beam charge of 2.3nC, a solenoid strength of 1420 Gauss, an RF injection phase of 40 degrees, and a cathode spot size of 0.2 cm, the bunch length was scanned between 2 and 20 degrees. It is expected that as the bunch length is shortened, the transverse emittance will increase because the space charge forces will be much greater. By shrinking the bunch length the longitudinal phase space is also shrinking, however the space-charge forces are increasing in the longitudinal direction as well. Similar to the spot size case for the transverse case we expect here that the longitudinal emittance will have a minimum at some nominal bunch length.. Figure 35 shows the longitudinal emittance as a function of the bunch length.

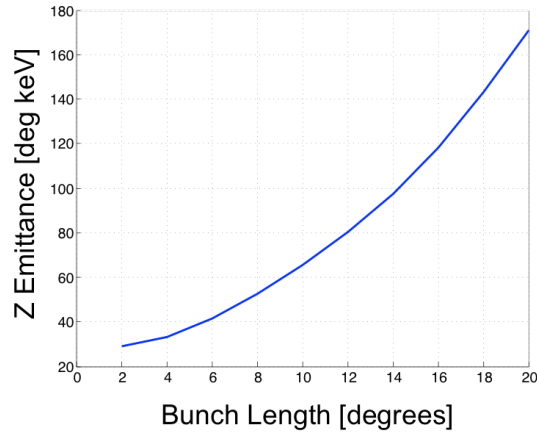


Figure 35: Longitudinal emittance as a function of the bunch length

Here the longitudinal emittance does decrease as the bunch length decreases, but does not reach a true global minimum. As the bunch length increases the phase space in this plane is increasing and therefore the emittance is similarly increasing. Analysis of the rate of change of emittance as a function of bunch charge shows that this rate is decreasing as the bunch length decreases, indicating a minimum does exist. The bunch length also affects the transverse emittance, shown by Figure 36.

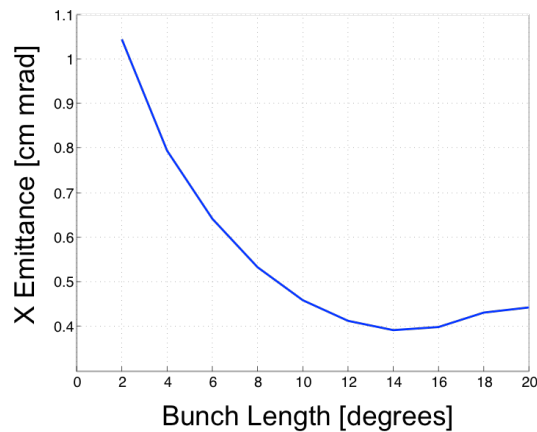


Figure 36: Transverse emittance as a function of the bunch length

As with the longitudinal emittance the transverse emittance behaves as is expected. There is a steady decrease in the emittance as the bunch length is increased. The emittance reaches a

minimum value at around 14 degrees and then increases slightly up to 20 degrees. This minimum in the emittance is expected as the solenoid is set to compensate for a particular beam current. As the bunch length is increased the beam current for a particular bunch charge is decreased. Therefore some point after the optimum the solenoid is actually over focusing the bunch and over compensating for the space-charge effects.

4.3 Injector point design

With a good understanding of how variations in the injector parameters affect the beam output, an initial configuration is provided to use for simulations of the beam-line in Chapter 5. These settings are given in Table 4.

Table 4: Beam parameters and injector parameters for a point design

Bunch Charge	2.3nC
RF Phase	40 Degrees
Bunch Length	40 ps
Solenoid Field	1420 Gauss
Beam Energy	6.3 MeV

Using PARMELA the injector was simulated with these parameters, which produces a beam with a normalized transverse emittance of 0.43 cm-mrad, and a longitudinal emittance of 147.4 degrees-keV. At the exit of the injector the beam has a spot size of 2 mm. PARGRAF, the PARMELA plotting program, computes the RMS Twiss parameters, given in Table 5. These parameters describe the behavior in the core of the beam, which are used in Chapter 5 as the primary input to the beam-line matching. The PARMELA input file used for these simulations is provided in Appendix C. Having a complete well-understood model of the CSU injector, a beam-line can be used to match these parameters to the undulator. This process is covered in detail in Chapter 5.

Table 5: Twiss parameters at the exit of the injector for the point design provided

α_x	2.7
β_x	220.0 [cm/rad]
α_y	2.7
β_y	226.6 [cm/rad]

5. Beam-Line Matching for the Undulator

The previous two chapters addressed modeling and simulation studies of the injector system. With that information the next step in developing a full machine model and initial system layout, is the beam transport and matching system for the undulator, which is developed in this chapter. To generate the initial layout the University of Twente provided a schematic system of the accelerator as it was when last operated. This gives a total length, seen by the beam, between the injector and the undulator of 153 cm. While this number may seem odd, it must account for the nonzero length of vacuum pipe between the start of the undulator vacuum pipe and the actual start of the undulator, 3cm. This total distance will lead to some seemingly strange drift lengths between quadrupoles. These numbers should therefore be used for fiducialization and don't represent suggested cut lengths of the vacuum tubes. Keeping this total length constant, the initial beam-line design will have 5 evenly spaced quadrupoles used to match the beam into the undulator. This allows for a system that should be relatively flexible for varying beam parameters.

The beam-line matching is done for the most part using two simulation tools, `elegant` [12] and `TRACE-3D` [13] (`TRACE`). `Elegant` is a particle-tracking code developed by Argonne National Laboratory and is used primarily for high-energy, electron beam systems. Space-charge forces are negligible at high energy therefore `elegant` does not need to account for these interactions. The CSU system is operating at a relatively low energy and the space-charge forces, while not dominating the beam, are still very much present. `TRACE`, on the other hand, does include a space-charge calculation in the code. `TRACE` is a Los Alamos developed code used for matching low-energy beams where space charge is still highly relevant. It functions similarly to `elegant`

in the use of transport matrices but has a slightly different interface. Unlike `PARMELA` both `TRACE` and `elegant` have built in optimization packages that are used for beam-line matching. Optimization routines are necessary when tuning beam-line elements, as good analytical solutions are difficult to work with. A combination of these two codes allows for some comparison to show just how much space charge is impacting the beam-line set points. Then for the initial set point design, `TRACE` is used to simulate the beam with space charge and these results are simulated in `PARMELA` to verify. Further tweaking is then done through the use of custom optimization routines that work directly with `PARMELA`. Before discussing the details of the beam-line simulations, an overview of `elegant` and `TRACE` is given to provide the reader with some context for the simulations performed in this chapter.

5.1 Overview of `elegant` and `TRACE-3D`

`Elegant` and `TRACE` are both particle tracking codes which utilize transfer matrices to analyze the beam as it propagates through a given lattice. The beam is tracked using the full 6D phase-space transfer matrices. The transport matrices are constructed based on the beam envelope equations described in Chapter 2. Both `elegant` and `TRACE` have built in optimization routines that are used for beam-line design and matching. With these routines the user can specify a number of constraints on the problem and define the starting point for the search space.

The beam parameters are input to both systems as RMS Twiss parameters. These are generated by `PARMELA` from the simulations in Chapter 4. The distinction that we use RMS parameters is important as it describes the behavior of the beam core and neglects the effects that create beam tails and halos. In the context of machine operation it is not possible to always control the beam

halo nor is it easy to measure it; however, measurement of the RMS parameters is more straightforward. Therefore, we are only concerned with this aspect of the beam for the point design.

For further discussion on `elegant` and `TRACE` consult their respective user manuals.

5.2 Beam-line Matching to the Undulator

In order to properly match the beam into the undulator the beam envelope must satisfy the proper conditions. For an undulator with equal focusing in both planes a proper match means the beta function in both planes must satisfy the following [14]:

(38)

$$\beta = \frac{\lambda_u \gamma}{K\pi}$$

Here λ_u is the undulator period, γ is the relativistic energy of the particle beam, K is the undulator normalized field parameter, and β is in reference to the envelope equation discussed in Chapter 2. For the CSU machine $K = 1$, $\gamma \approx 13$ and $\lambda_u = 0.025$. Substituting these parameters into Equation 36 gives beta functions equal to 0.106 [m/rad] to properly match the beam. Implicit in a beam matched into the undulator is a zero phase-space tilt. For the purposes of this design, a satisfactory match is within 5% of the target value for the beta functions, and alpha functions as small as reasonably achievable. These parameters specify the target values and their tolerances for both `TRACE` and `elegant` to match by varying the upstream quadrupoles. The lattice used for the matching consists of five equally spaced quadrupoles with drift spaces in between. The drift spaces provide room for beam position monitors and correctors as well as

diagnostics. Additionally they provide space for the beam to evolve before making an adjustment with the quadrupoles. Table 6 shows the initial beam-line elements including quadrupole locations and their initial settings. The quadrupole starting points were chosen pseudo-randomly such that the beam should behave well when propagating down the beam-line. All distances are given in meters and field gradients are given in terms of the PARMELA standard, which has units of Gauss/cm.

Table 6: Beam line elements and positions for the starting point to the `elegant` optimization lengths and positions are given in meters and the field gradient is given in gauss/cm.

	Start Position	Length	dB/dx
Drift	0	0.20917	
Quadrupole	0.20917	0.055	-50
Drift	0.26417	0.20917	
Quadrupole	0.47334	0.055	50
Drift	0.52834	0.20917	
Quadrupole	0.73751	0.055	-50
Drift	0.79251	0.20917	
Quadrupole	1.00168	0.055	50
Drift	1.05668	0.20917	
Quadrupole	1.26585	0.055	30
Drift	1.32085	0.20917	

The initial beam parameters were taken from the injector simulations in the previous chapter and the target parameters were defined above. These are the RMS twiss parameters used in the optimization. These parameters are given explicitly in Table 7.

Table 7: RMS twiss parameter starting values and target values for the beam-line tuning in

	Initial Parameter	Target Value
Alpha X	2.66	0
Beta X	2.10 [m/rad]	0.1060 [m/rad]
Alpha Y	2.62	0
Beta Y	2.17 [m/rad]	0.1060 [m/rad]

With a set of initial beam and beam-line parameters the optimization to match the beam into the undulator can be performed. This is a multi-step process; first the beam-line is matched using `elegant`, then matched in `TRACE-3D` without space charge, and then in `TRACE-3D` with space charge. Following this, `TRACE-3D` is run iteratively with `PARMELA` to tweak the settings, and any further tweaking is done through custom optimization routines built to work directly with `PARMELA`. The purpose of `elegant` and `TRACE-3D` without space charge is to check that the beam core is indeed behaving as desired when comparing with `PARMELA`. The first step of simulating in `elegant` is to match the beam to the undulator. This gives the quadrupole settings that can be translated to `PARMELA`, which does a full beam simulation. The beam parameters from `elegant` are then compared to `PARMELA` both with and without space charge. The results of these simulations are shown in Figure 37.

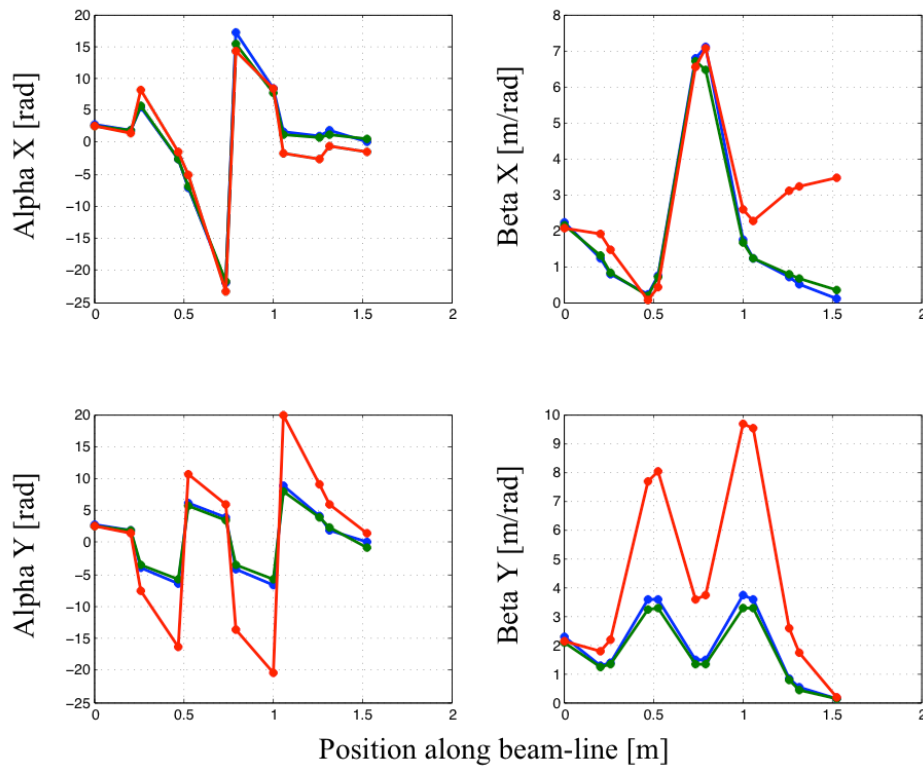


Figure 37: Comparison of the Twiss parameters for `elegant` and `PARMELA`. Blue is `elegant`, green is `PARMELA` without space-charge, and red is `PARMELA` with space-charge.

Here all four twiss parameters are compared for the three different simulations. It is clear that the `elegant` simulation and the `PARMELA` simulation without space-charge match very well. This shows that when space charge is off the centroid of the beam is behaving as expected. When space charge is turned on, however, the result is much different. The shape is generally the same; but, the match in the X direction is degraded significantly and is no longer being properly focused. Additionally the alpha functions are no longer properly matched. This shows that, as expected, space-charge plays a significant role in the beam-line matching. In order to account for these effects `TRACE` can be used to match the beam with space-charge. First `TRACE` is used to simulate the beam without space charge. This provides a starting point for the `TRACE` optimization with space charge. These results are shown in Figure 38.

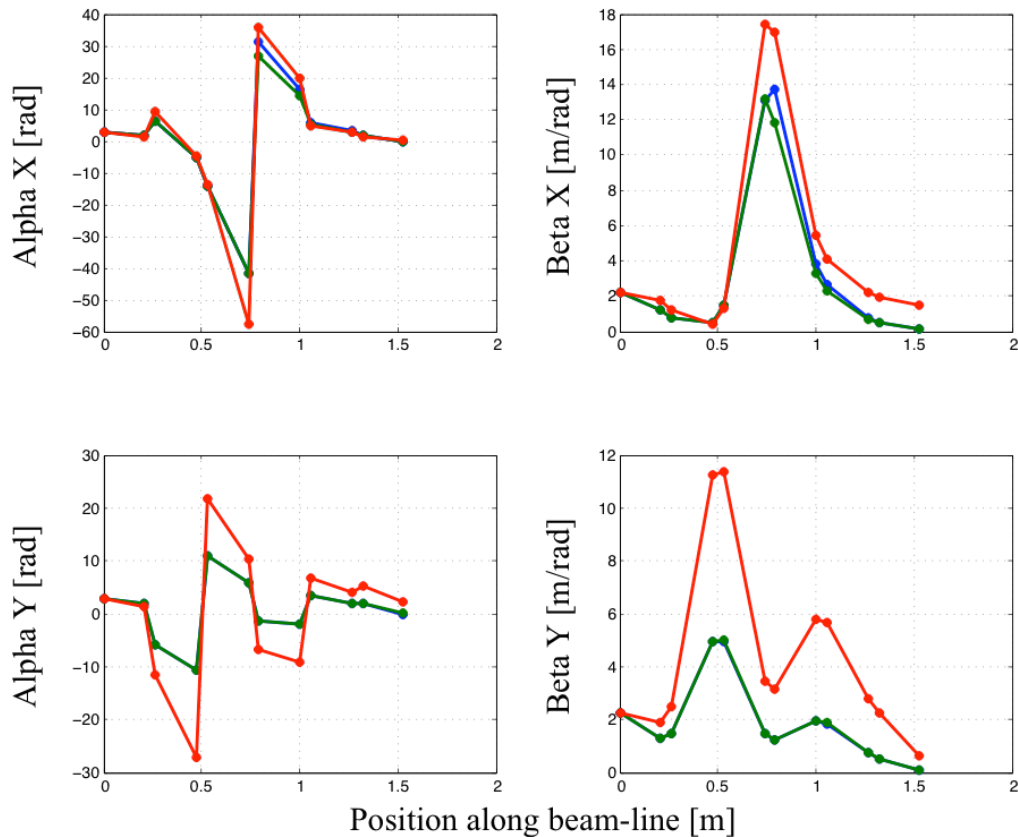


Figure 38: Comparison of the Twiss parameters for `TRACE` and `PARMELA`. Blue is `TRACE` without space charge, Green is `PARMELA` without space-charge and Red is `PARMELA` with space-charge.

Here as before the simulations with space charge off match very well. Additionally, as before, once space charge is turned on the match degrades and is no longer at the desired values. A comparison of the Twiss parameters, shown in Table 8, for each of the cases in Figure 38 shows how poor the match is once space charge is introduced.

Table 8: Comparison of Twiss parameters with TRACE and PARMELA to the target values. PARMELA is simulated both with and without space-charge using the beam-line settings provided from the TRACE optimization.

	TRACE w/o space-charge	PARMELA w/o space-charge	PARMELA w/ space-charge	Target
Alpha X	-2.48e-06	-4.9e-2	0.37	0
Beta X	0.106 [m/rad]	0.120 [m/rad]	1.5272 [m/rad]	0.106 [m/rad]
Alpha Y	8.84e-06	3.6e-3	2.29	0
Beta Y	0.106 [m/rad]	0.104 [m/rad]	0.634 [m/rad]	0.106 [m/rad]

In order to correct these errors, the TRACE optimization is run with space-charge on to adjust the beam parameters for the undulator. The settings produced are then implemented in PARMELA to verify the result. The results of these simulations are shown in Figure 39. Here a visual inspection of the plots shows that PARMELA and TRACE are in reasonable agreement. In order to verify that the match is satisfactory, Table 9 compares the twiss parameters from both TRACE and PARMELA , to the target values.

Table 9: Twiss parameters at the entrance to the undulator from TRACE and PARMELA

	TRACE Result	PARMELA Result	Target Value
Alpha X	8.4e-06	0.56	0
Beta X	0.106 [m/rad]	0.215 [m/rad]	0.106 [m/rad]
Alpha Y	1.2e-05	0.38	0
Beta Y	0.106 [m/rad]	0.144 [m/rad]	0.106 [m/rad]

While the beam parameters in PARMELA are much closer to the target value compared to the elegant simulations and the TRACE simulations without space charge, there is still quite a bit of error between the desired match point and the simulation results. This is likely due to insufficient space charge current in the TRACE simulations. A visual inspection of figures 37 and

38 show that when space charge is on vs. off the magnitude of the beta and alpha functions is smaller and larger respectively while maintaining the same shape. This same result is visible in Figure 39 when comparing TRACE and PARMELA.

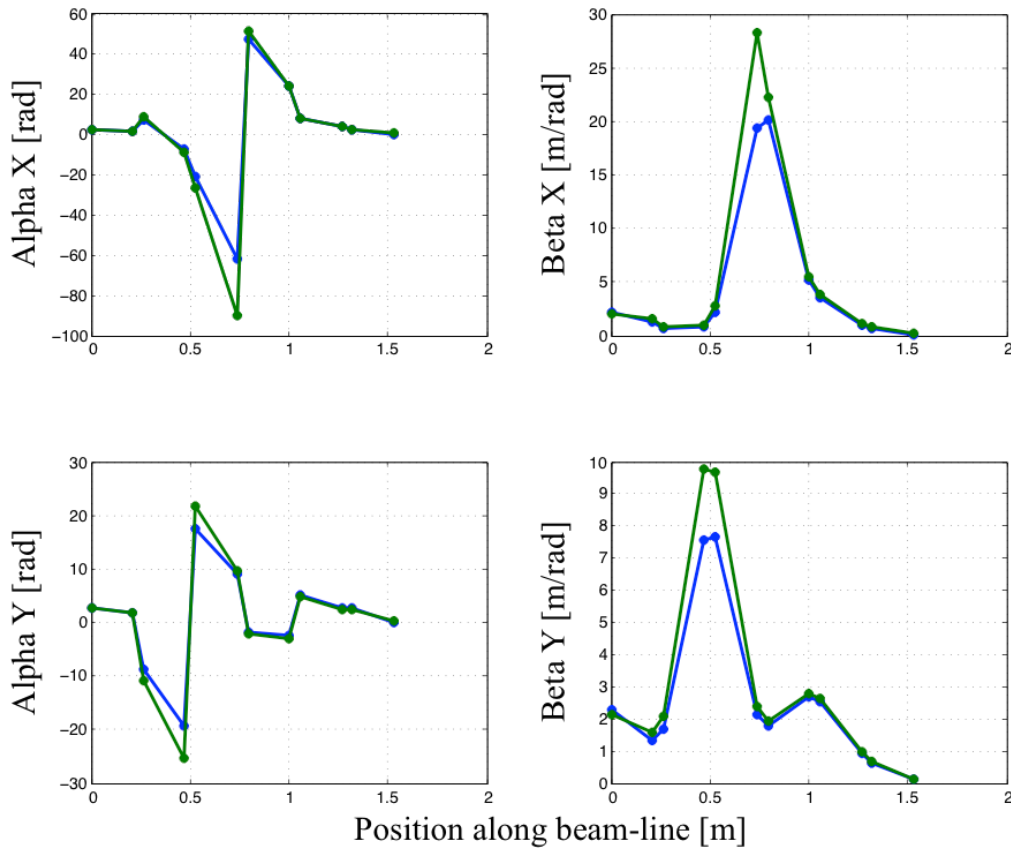


Figure 39: Comparison of the Twiss parameters for TRACE and PARMELA. Blue is TRACE with space charge turned on, green is PARMELA with space-charge on.

To verify this, the space charge current in TRACE was systematically increased, and the beam-line was re-matched. The settings from TRACE were then simulated in PARMELA to verify. This process showed that indeed TRACE was not adequately accounting for all the space charge in PARMELA. In order to produce a better match, TRACE was run iteratively with PARMELA while slowly increasing the space charge until the Twiss parameters were closer to the target. After a few iterations, the beam was much better matched and the results are presented in Table 10.

Table 10: Beam parameters from PARMELA simulation with beam-line settings from iteration of TRACE and PARMELA

	TRACE Result	PARMELA result	Target Value
Alpha X	5.0e-5	-0.133	0
Beta X	0.106 [m/rad]	0.118 [m/rad]	0.106 [m/rad]
Alpha Y	-4.8e-6	-0.308	0
Beta Y	0.106 [m/rad]	0.100 [m/rad]	0.106 [m/rad]

This solution brings the PARMELA match much closer than was shown in Table 9. The beta functions, however, still have an 11% error from the desired value. In order to further tweak the beam-line an optimization routine was programmed to work directly with PARMELA input and output. These custom developed scripts utilize the gradient descent method, chosen for its ease of implementation, to adjust the quadrupole strengths and further reduce the error in the beta functions. After a few iterations the optimization routine was able to successfully tweak the beam-line to be matched within 2% for the beta functions, the results of which is shown Table 11.

Table 11: Final beam parameters from custom PARMELA optimization routine

	Final Parameter	Target Value
Alpha X	-0.6676	0
Beta X	0.1066[m/rad]	0.106 [m/rad]
Alpha Y	-0.0443	0
Beta Y	0.1078 [m/rad]	0.106 [m/rad]

As an aside it is important to note how minor the changes are to tweak from Table 10 to Table 11. For a real system the beam must be matched as well as possible and depending on the resolution of the source used to power the magnets, these changes may be below practical limits. Table 12 shows a comparison of the two different beam-line settings. For a high degree of accuracy in the match, a high degree of accuracy in the quadrupole settings is required.

Table 12: Comparison of beam-line settings produced from TRACE iterations to full simulation optimization

	Table 10 Settings	Table 11 Settings
Quad 1	-299.097	-299.190
Quad 2	201.094	201.009
Quad 3	-225.389	-225.986
Quad 4	124.396	124.889
Quad 5	32.062	32.485

In order to verify the match is satisfactory the output of the undulator is checked. If the beam is well matched into the undulator, then the beam parameters at the exit of the undulator should be very close to the parameters at the entrance. The undulator is simulated in PARMELA and the initial vs. final twiss parameters are shown in Table 13.

Table 13: Pre and Post wiggler twiss parameters

	Pre Wiggler	Post Wiggler
Alpha X	-0.6676	0.377
Beta X	0.1066[m/rad]	0.112 [m/rad]
Alpha Y	-0.0443	-0.248
Beta Y	0.1078 [m/rad]	0.147 [m/rad]

This shows that the beam is relatively well matched to the wiggler. Note that if the input beam had smaller alpha functions the output beam would be better matched to the input beam. This is because the alpha function represents a change in the beta function, therefore the beta function may be matched at the entrance to the wiggler but it is still changing. In order to fine-tune these parameters a higher resolutions series of full optimizations in PARMELA with tighter tolerances on the parameters would be necessary. The beam-line description, which resulted from the matching with the quadrupole strengths specified, is given in Table 14.

Table 14: Beam-line set points and locations for the matched system. Note that the zero point of the beam line is the exit of the injector.

	Start Position	Length	dB/dx
Drift	0	0.20917	
Quadrupole	0.20917	0.055	-299.190
Drift	0.26417	0.20917	
Quadrupole	0.47334	0.055	201.009
Drift	0.52834	0.20917	
Quadrupole	0.73751	0.055	-225.986
Drift	0.79251	0.20917	
Quadrupole	1.00168	0.055	124.889
Drift	1.05668	0.20917	
Quadrupole	1.26585	0.055	32.485
Drift	1.32085	0.20917	

This section has focused on how to match the beam-parameters prescribed by the previous chapter to the undulator using `TRACE`, `elegant`, and custom built direct `PARMELA` optimization scripts. Additionally this section has shown that the `TRACE` code with space charge produces a very close result to the `PARMELA` simulations but for a high quality match a custom optimization routine which works directly with `PARMELA` must be employed. This shows that for a particular input specified in Chapter 4, the beam-line design can adequately match the envelope parameters to the undulator. It is important to also consider how robust the beam-line is to variations in the input beam parameters. In order to investigate this the input beam parameters are varied and the result of the beam-line match studied.

5.3 Matching sensitivity to input beam parameters

The previous section showed that `TRACE` produces a satisfactory match that is within 11% when replicated with `PARMELA`. It is implicit that results from `TRACE` would need to be tweaked further

but the TRACE results do represent, from a broad standpoint, how robust the system is to changes in the input beam parameters.

To assess this, the input beam parameters were varied for 8 different sets of parameters and the match using TRACE was performed. For every case TRACE was able to match the beam exactly. As shown in the previous section, even if TRACE gives a near perfect match, due to the use of analytic approximations for the beam envelope the real parameters will be slightly off. However, this should get to within 10% of the desired value. The parameters from TRACE can then be used in a full simulation optimization, as with the previous section, to tweak the beam-line settings such that the desired match will be achieved.

The cases studied were broken into four subcategories, large beta with small alpha where the transverse planes are matched, large beta and small/modest alpha where the beta functions are matched but the alpha functions are mismatched, large/modest beta functions with small/modest mismatch, and large/modest alpha and beta functions with large/small mismatch in both planes.

The results of these simulations are presented in Tables 15-18.

Table 15: Results from TRACE match for a large beta and a small matched alpha.

	Initial	Final	Initial	Final
Alpha X	0	-3.7E-05	1	4.4e-5
Beta X	5	0.1060	5	0.1060
Alpha Y	0	-3.9E-06	1	-2.7e-6
Beta Y	5	0.1060	5	0.10601

Table 16: Results from TRACE match for a large beta and a small/modest mismatched alpha.

	Initial	Final	Initial	Final
Alpha X	-1	1.7e-5	-3	-1.4e-5
Beta X	5	0.1060	5	0.1060
Alpha Y	1	-9.2e-6	3	1.4e-6
Beta Y	5	0.1060	5	0.1060

Table 17: Results from TRACE match for a large/modest mismatched beta and a small matched alpha.

	Initial	Final	Initial	Final
Alpha X	1	-2.8e-6	1	1.4e-6
Beta X	5	0.1060	5	0.1060
Alpha Y	1	-9.6e-6	1	1.9e-5
Beta Y	4	0.1060	2	0.1060

Table 18: Results from TRACE match for a large/modest mismatch in beta and alpha

	Initial	Final	Initial	Final
Alpha X	1	-1.1e-5	1	4.4e-6
Beta X	5	0.1060	5	0.1060
Alpha Y	-1	-2.1e-5	-3	-3.8e-7
Beta Y	4	0.1060	2	0.1060

These results show that the beam-line is robust to changes in the beam parameters and can match various beams to the undulator in addition to correcting for significant mismatch in the transverse beam parameters. While any settings produced from these simulations would require additional tweaking in either simulation or in startup, for a given set of input beam parameters the design presented here can adequately manipulate the beam to the desired parameters for FEL operation.

During this chapter the beam-line was designed and simulated using `elegant` and `TRACE-3D`. With the use of these two codes, and `PARMELA` as a check, the final beam-line matching section was shown and provided for the initial system setup. With this design, and a simulation of the undulator, the downstream beam line can be tuned and then used in a full start-to-end simulation of the CSU accelerator system.

6. Spectrometer Diagnostic Optimization

After the wiggler, it is necessary to analyze the energy spectrum of the beam. This is done through the use of a spectrometer dipole. In Chapter 2 it was noted that the bend radius of a particle traveling through a constant magnetic field is proportional to the energy of the particle. For a particle beam with some spread in the energy the various energies will have different path lengths through the dipole and thus create a correlation between the spread in the bend plane and the spread in energy, called dispersion. For a particular spectrometer, the dispersion in the beam due to the energy spread is the bend angle multiplied by the length of drift following the magnet. The CSU spectrometer has a bend angle of 90 degrees ($\pi/2$ radians) and a drift of 0.5 m. This yields an expected dispersion of 0.78-m. It is desirable to resolve down to three significant figures in the energy spectrum. For a dispersion of 0.78-m, the smallest feature resolved by the camera would need to be 0.78mm. Modern cameras should be able to identify features this small; however, the beam spot size due to emittance must be smaller than this limit in order to not affect the measurement. Recall that the beam spot size is determined by the emittance and the beta function, therefore in order to satisfy this spot size condition, the beta function must be less than 0.195 m/rad.

The bending magnet is in the vertical (y) plane and therefore dispersion will only occur in this plane, thus the resolution of the spectrometer depends solely on the vertical beta function. The horizontal (x) beta function, however, must still be monitored to prevent the beam from scraping the beam-pipe. The alpha functions which describe the change in the beta function, are less important in this case as once the energy spectrum is recorded, the beam is dumped. This gives

one parameter to be optimized and one parameter to be controlled, which require a minimum of two quadrupoles. This will be used as a starting point design, given by Table 19.

Table 19: Starting Points for the Post Undulator Lattice. Note the positions are given in meters relative to the exit of the undulator and the quadrupole field strengths are given in gauss/cm. Note the length of the bend is the total path length seen by the reference trajectory, corresponding to the bend radius multiplied by the bend angle.

	Start Position	Length	dB/dX
drift	0	0.145	
quad	0.145	0.055	113
drift	0.2	0.050	
quad	0.25	0.055	-113
drift	0.305	0.145	
bend	0.45	0.471	
drift	0.921	0.500	

Both `elegant` and `TRACE` were used to determine the quadrupole set points. First `elegant` was used to optimize the beam-line without space charge, then the resulting quadrupole settings were simulated and tweaked with `TRACE`, to include the effects of space-charge. This two-step process is necessary because `TRACE` has a less flexible optimization routine that does not allow for the alpha functions to be ignored while optimizing the beta functions. `Elegant` on the other hand, has the ability to treat these separately. The result from `elegant` was verified in `PARMELA` without space charge. These results are shown in Figure 40.

Here there is very good agreement in the non-bending plane (β_{x}) and decent agreement in the bend plane (β_{y}). In both cases the beta functions are small enough such that the beam will not scrape the beam-pipe. The final vertical beta function is 0.06, well within the limits for the desired resolution. The quadrupole parameters from the `elegant` optimization were then transferred into `TRACE` to make adjustments for the inclusion of space-charge. Figure 41 shows

the results from TRACE and the corresponding quadrupole settings simulated in PARMELA, both with space charge on.

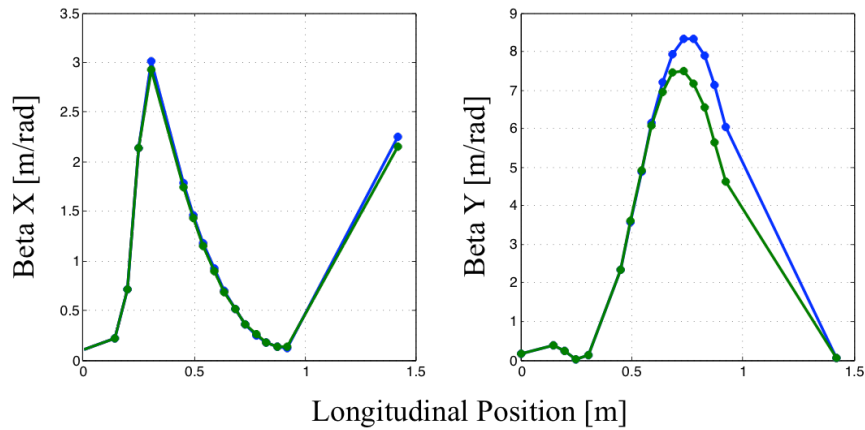


Figure 40: Transverse beta functions in post wiggler beam-line. Green is PARMELA without space charge, blue is elegant without space charge. Note the dipole is broken up into 10 segments to allow for higher resolution in these figures.

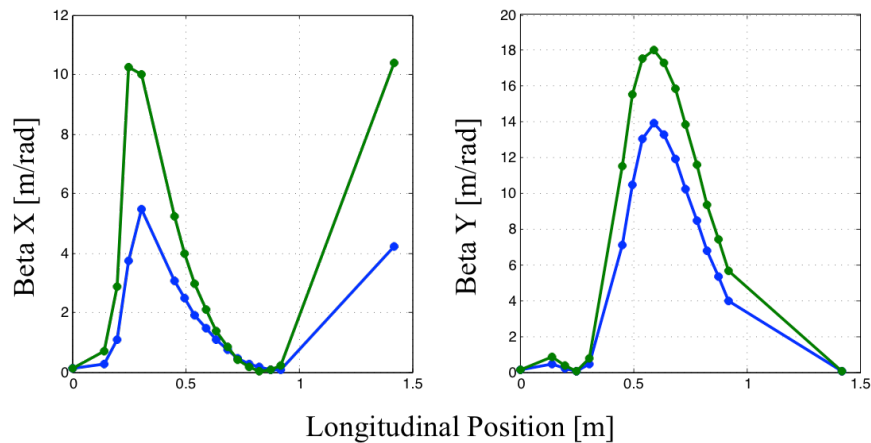


Figure 41: Transverse beta functions in post wiggler beam-line. Green is PARMELA with space-charge, blue is TRACE with space-charge. Note the dipole is broken up into 10 segments to allow for higher resolution in these figures.

Here the two simulations do not agree nearly as well as Figure 40, but there is still a reasonable agreement between TRACE and PARMELA. Additionally the parameter of importance, the vertical beta function at the end of the beam-line, matches very well comparing TRACE to PARMELA. The corrected beta function after simulating the beam-line settings from TRACE in PARMELA is 0.077,

well within the desired value for the required resolution. Note that this result is for the post wiggler section simulated in absence of the rest of the machine, when simulated with the whole beam-line the RMS beam spot size was 0.9mm. Full machine optimization runs could tweak this down to within the threshold however for initial buildup this result is satisfactory. The dispersion function through the dipole is also computed to show the energy/position correlation expected on the screen, this is presented in Figure 42.

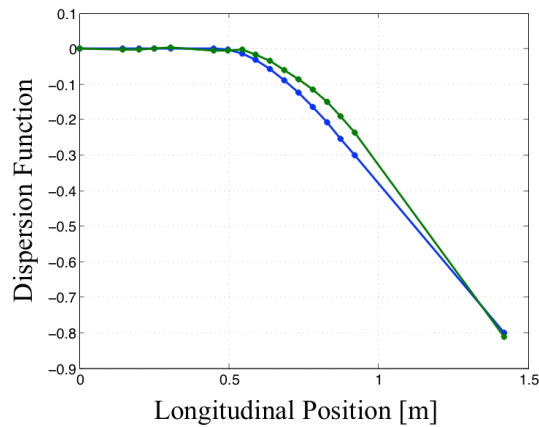


Figure 42: Vertical (y) dispersion along the post wiggler beam-line. Blue is from the elegant simulation, green is from the final PARMELA simulation with space charge on

Here there is very good agreement, as expected, in the two dispersion calculations. Additionally the dispersion at the screen is about 0.8 very close to the calculated value from before. Table 20 gives the final beam-line settings for the post wiggler beam-line and spectrometer.

Table 20: Post wiggler beam line settings. Note field gradients are given in terms of gauss/cm

	Start Position	Length	dB/dX
drift	0	0.145	
quad	0.145	0.055	871.908
drift	0.2	0.050	
quad	0.25	0.055	-412.676
drift	0.305	0.145	
bend	0.45	0.471	
drift	0.921	0.500	

7. Start to end beam simulations and startup layout

During the last four chapters models and simulations of the individual accelerator components have been developed. Now it is possible to combine these into a complete start-to-end simulation. This covers the accelerator, beam-line, undulator, and spectrometer. The start-to-end simulation is done in PARMELA using the settings and locations from Chapter 5 and 6, combined with the settings from Chapter 4, and the models from Chapter 3. The initial beam properties correspond to 2.3-nC of charge, a 40-ps bunch length, and a 2 mm cathode spot size. The simulation results are presented in terms of the transverse envelope parameters, the transverse emittance, and the longitudinal emittance. Finally the beam-line locations are defined explicitly referenced to the beginning of the accelerator and the necessary set points are listed. Figure 43 shows the transverse beta functions along the length of the accelerator.

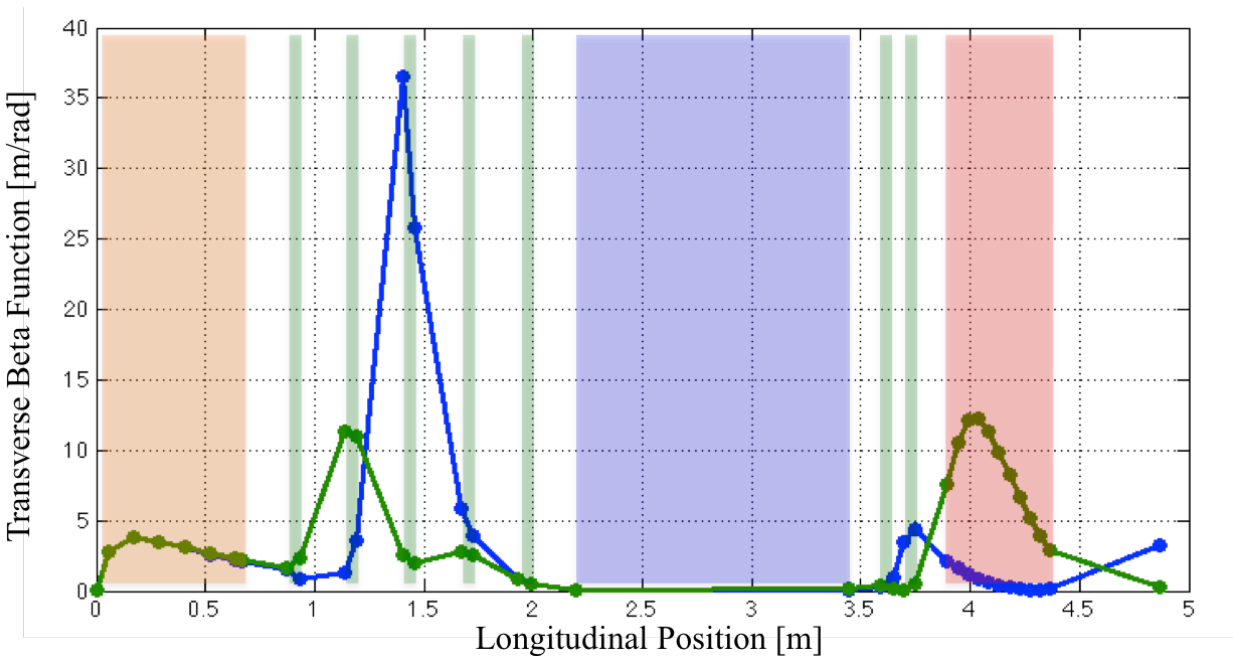


Figure 43: Transverse beta functions as a function of position along the accelerator. X beta function is in blue, Y beta function is in green. Accelerator components are highlighted in the following manner; orange (injector), green (quadrupoles), blue (undulator), and red (spectrometer).

As the beam propagates through the system, the envelope varies significantly. During the injector portion the transverse beta functions are equal due to symmetry, and are decreasing as the beam moves toward the beam-line. The parameters are then adjusted using the quadrupoles to match the beam for the undulator. During transport through the undulator the beam envelope is relatively unchanged as expected for this system. After the undulator the beam envelope is re-focused for the spectrometer shown at the end of the beam-line. As in Chapter 6, the vertical beta function is at a minimum for the spectrometer screen and the beam dump. The transverse alpha function, presented in Figure 44, provides additional information about the beam phase space.

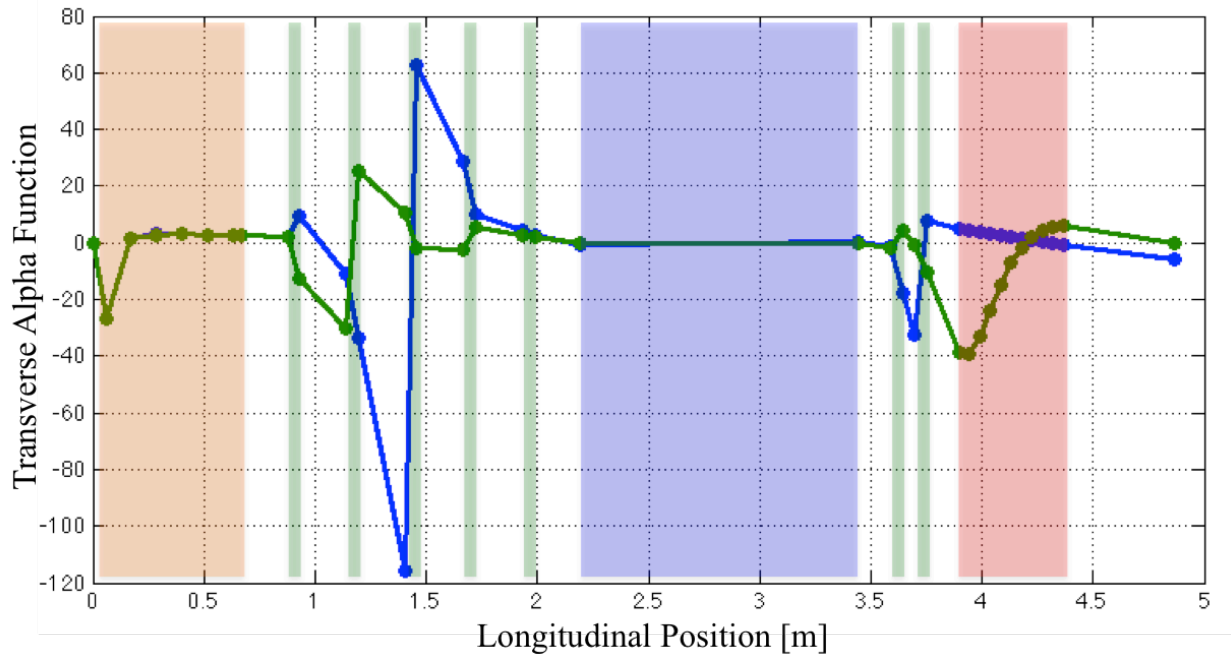


Figure 44: Transverse alpha functions as a function of position along the accelerator. X alpha function is in blue, Y alpha function is in green. Accelerator components are highlighted in the following manner; orange (injector), green (quadrupoles), blue (undulator), and red (spectrometer).

In the injector both the transverse alpha functions are, as with the beta functions, equal to one another. The beam-line then adjusts the alpha functions such that they are matched into the undulator. Again, as with the beta functions, the input alpha functions to the undulator are very

close to those of the output. Down-stream of the undulator these parameters are adjusted for the spectrometer.

Information about the beam quality is also necessary to study how the beam evolves along the accelerator. To address this, Figure 45 shows the emittance along the accelerator.

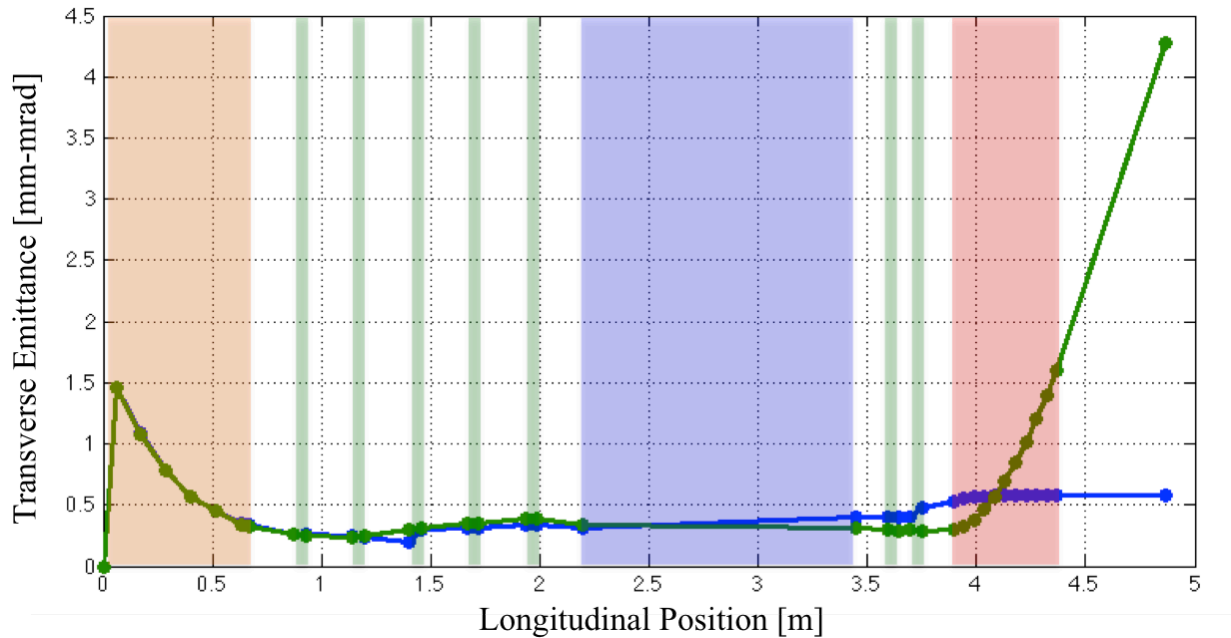


Figure 45: Transverse emittance functions as a function of position along the accelerator. X emittance function is in blue, Y emittance function is in green. Accelerator components are highlighted in the following manner; orange (injector), green (quadrupoles), blue (undulator), and red (spectrometer).

The beam quality varies along the system and gives an idea of what qualities to expect in the undulator. This is helpful when calculating FEL gain. Note that previously it was discussed that emittance is conserved and therefore should be unchanged. This is not in general true for the RMS quantities. It is expected that the emittance will peak in the injector and then again peak in the bend plane of the spectrometer. It should remain relatively constant elsewhere along the beam-line. This is supported by the results here. In addition to the transverse emittance, the longitudinal emittance must also be considered. While the CSU beam-line is not setup to perform

manipulations to the longitudinal phase space, it is good to verify that nothing unexpected is happening along the accelerator. Figure 46 shows the longitudinal emittance as the beam propagates through the system.

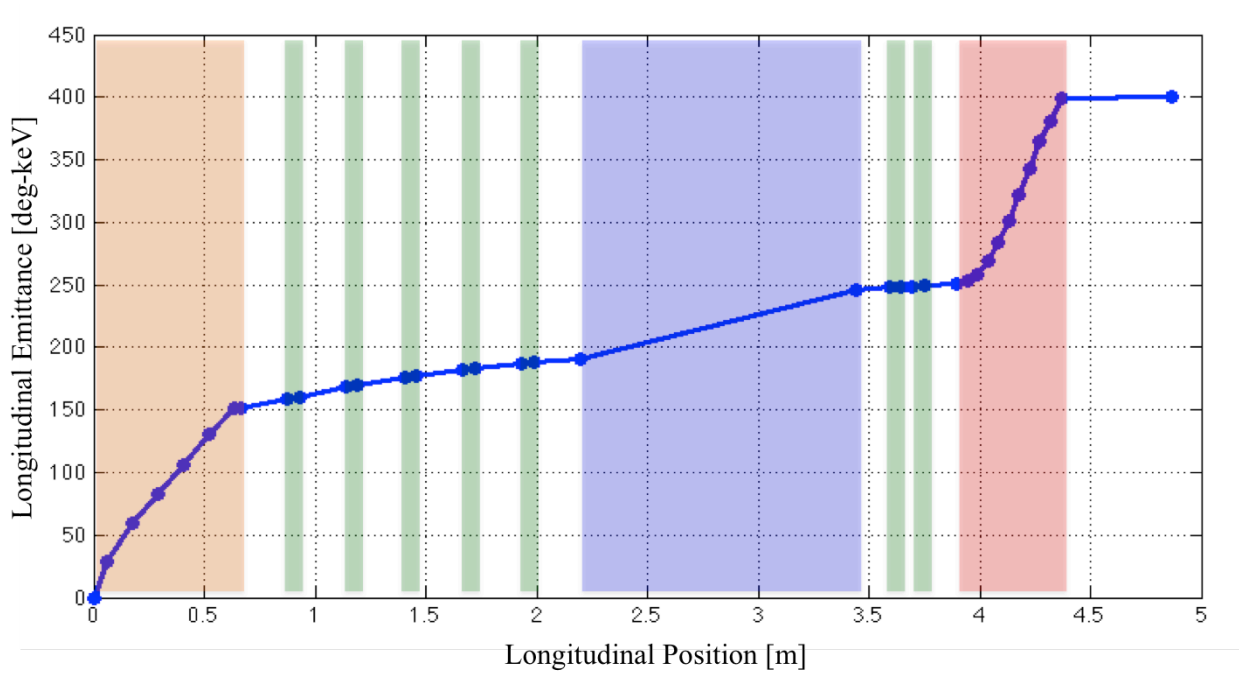


Figure 46: Longitudinal emittance functions as a function of position along the accelerator. Accelerator components are highlighted in the following manner; orange (injector), green (quadrupoles), blue (undulator), and red (spectrometer).

There should be little change to the longitudinal phase space except in the acceleration section (orange part of Figure 46), and in the dipole (red part of figure 46). This is more or less verified by the results shown. The longitudinal emittance changes the most in the injector; however, there is some not insignificant growth in the longitudinal emittance along the beam-line cause by the remaining, non-zero space charge forces. The set points and beam-line element locations used to create this model are given in Table 21. Additionally the PARMELA file used for this simulation is given in Appendix C.

Table 21: Beam-line locations and set points. Positions are referenced to the beginning of the accelerator in meters; quadrupole set points are given in gauss/cm.

Element	Start	Length	Setting
Linear Accelerator	0	0.66577	N/A
Drift	0.66577	0.20917	
Quadrupole	0.87494	0.055	-299.190
Drift	0.92994	0.20917	
Quadrupole	1.13911	0.055	201.009
Drift	1.19411	0.20917	
Quadrupole	1.40327	0.055	-225.986
Drift	1.45827	0.20917	
Quadrupole	1.66744	0.055	124.889
Drift	1.72244	0.20917	
Quadrupole	1.93161	0.055	32.485
Drift	1.98661	0.20917	
Undulator	2.19577	1.25	
Drift	3.44577	0.145	
Quadrupole	3.59077	0.055	871.908
Drift	3.64577	0.050	
Quadrupole	3.79077	0.055	-412.676
Drift	3.84577	0.145	
Bend	3.99077	0.47124	
Drift	4.46201	0.500	

This thesis has provided the details of an initial beam-line design that adequately manipulates the beam properties from the injector to the required beam properties for the undulator, and focuses the beam to achieve high resolution in the spectrometer. Beginning with the relevant background and subsequently examining each component of the accelerator independently provides a demonstration of how this design will operate. Electromagnetic models of the accelerator combined with detailed simulations of the injector show how the system will perform under a variety of operating conditions. The undulator-matching beam-line was then studied for robustness. This revealed that a wide range of injector outputs could adequately be matched to the undulator. Finally, the down-stream beam-line was analyzed to show how the beam should

be focused such that the spectrometer can properly diagnose the beam energy spectrum. With the set points and positions provided here, the accelerator system can now be assembled for proper operation.

There are several important additional steps that must be completed in the machine characterization and simulation process. The first of these is to introduce alignment errors and offsets such that the position of beam-position-monitors, corrector magnets, and other diagnostics can be determined. Additionally a simulation of the RF cavity that captures the asymmetries not modeled in this thesis can be performed utilizing a 3-D accelerator code. These models would provide a more detailed description of the accelerator system and can be compared to the simulations presented here to assess how the additional simulation accuracy impacts the beam simulations.

Any future experiment that will utilize the CSU accelerator and beam-line can first be simulated with the models presented in this thesis. Novel electron gun designs can provide an input beam distribution to the accelerator system, thus treating the 5.5 cell structure as a booster. This would provide details on how a different electron source would perform if tested in the CSU beam-line. Similarly, diagnostics can be tested using the beam parameters and distributions at a particular position along the beam line that would provide insight to how the diagnostic would perform once implemented in the accelerator. Furthermore, beam-line elements, such as chicanes, novel magnets, kickers etc., can be simulated using the models in this thesis to show how they might perform in the system. Control systems could also be developed with these simulations before implementation on the accelerator. Virtually any experiment that utilizes the beam-line as a

workbench would begin by using these simulations to study performance with the existing system. In conclusion, this thesis provides a detailed starting point for both the buildup process and for future experiments that intend to utilize the CSU machine.

References

- [1] Kwang-Je Kim, “RF and Space Charge Effects in Laser Driven RF Electron Guns” Nuclear Instruments and Methods in Physics Research A275 (1987) 201-208
- [2] Klaus Wille, “The Physics of Particle Accelerators an Introduction” Oxford University Press 2000
- [3] D. A. Edwards and M. J. Syphers “An Introduction to the Physics of High Energy Accelerators” Wiley Series in Beam Physics and Accelerator Technology, 2004 Wiley-VHC
- [4] Thomas Wangler “RF Linear Accelerators” Wiley Series in Beam Physics and Accelerator Technology, 1998 Wiley
- [5] Carlsten, “New Photoelectric Injector Design for the Los Alamos National Laboratory XUV FEL Accelerator” Nuclear Instruments and Methods in Physics Research A285 (1989) 313-319
- [6] Martin Reiser, “Theory and Design of Charged Particle Beams” Wiley Series in Beam Physics and Accelerator Technology, 1994 Wiley
- [7] P. M. Lapostolle, IEEE Ttrans Nuclear Science NS-18 (1971) 1101-1104
- [8] J. Billen “Poisson Superfish Codes”, Los Alamos National Laboratory, Copyright 1985-2005
- [9] D.L. Schrage, L.M. Young, D.J. A&in, W.L. Clark, R.F. DePaula, C. Gladwell, F.A. Martinez, A.C. Naranjo, P.L. Roybal and J.E. Stovall “University of Twente Photocathode Linac” Nuclear Instruments and Methods in Physics Research B79 (1993) 721-725
- [10] L. Young “PARMELA Codes” Los Alamos National Laboratory, Copyright 1985-205
- [11] J.P. Edelen et. all “Electron Back-bombardment and mitigation in a short gap thermionic cathode RF Gun” IEEE Transactions in Nuclear Science, Volume 61 Issue 2.
- [12] M. Borland “ELEGANT (ELEctron Generation ANd Tracking)” Argonne National Lab
- [13] K. R. Crandall and D. P. Rusthoi “TRACE-3D” Los Alamos National Laboratory, May 1997
- [14] J. B. Murphy “Synchrotron light source data book” AIP Conference Proceedings 249 , 1939 (1992); doi: 10.1063/1.41969

Appendix A: SUPERFISH Cavity Input Files

A.1 Cell-1

University of Twente First Linac Cell

This is a half cell

® KPROB = 1,

ICYLIN=1,

FREQ = 1300,

DX = .02

xdri=1.0,

ydri=2.0,

conv=2.54,

beta=0.8

&

\$po x=0, y=0\$

\$po x=0, y=3.4269\$

\$po x=.748, y=3.4269\$

\$po nt=5, x=1.929, y=2.244, Radius=1.181\$

\$po x=1.929, y=1.6145\$

\$po nt=5, Radius=0.25, x=1.7925, y=1.392 \$

\$po nt=4, Radius=.394, x=1.517, y=1.017\$

\$po x=1.517, y=0.9915\$

\$po nt=4, Radius=.395, x=1.614, y=0.7325\$

\$po x= 1.654 ,y= 0.681 \$

\$po x= 1.693 ,y= 0.6375 \$

\$po x= 1.732 ,y= 0.5945 \$

\$po x= 1.772 ,y= 0.559 \$

\$po x= 1.811 ,y= 0.5275 \$

\$po x= 1.85 ,y= 0.504 \$

\$po x= 1.89 ,y= 0.488 \$

\$po x= 1.929, y=0.4765 \$

\$po x= 1.969, y=0.4725 \$

\$po x=2.27,y=.4725\$

\$po x=2.27,y=0\$

\$po x=0,y=0\$

A.2 Cell-2

University of Twente Second Linac Cell

® KPROB = 1,

ICYLIN=1,

FREQ = 1300,

DX = .02

xdri=2.27,

ydri=2.244,

conv=2.54&

\$po x=0,y=0\$

\$po x=0,y=0.4765\$

\$po x=0.341,y=0.4765\$

\$po x=0.38,y=0.488\$

\$po x=0.42,y=0.504\$

\$po x=0.459,y=0.5275\$

\$po x=0.498,y=0.559\$

\$po x=0.538,y=0.5945\$

\$po x=0.577,y=0.6375\$

\$po x=0.616,y=0.681\$

\$po x=0.656,y=0.7475\$

\$po nt=4, Radius=.395,x=0.753,y=.9915\$

\$po x=0.753, y=1.017\$

\$po nt=4, Radius=.395,x=0.4775,y=1.392\$

\$po nt=5,Radius=.25,x=0.341,y=1.6145\$

\$po x=0.341,y=2.244\$

\$po nt=5, Radius=1.181, x=1.522,y=3.4275\$

\$po x=2.27,y=3.4275\$

\$po x=3.018, y=3.4275\$

\$po nt=5, x=4.199, y=2.244, Radius=1.181\$

\$po x=4.199, y=1.6145\$

\$po nt=5, Radius=0.25, x=4.0625, y=1.392 \$

\$po nt=4, Radius=.394, x=3.787, y=1.017\$

\$po x=3.787, y=0.9915\$

\$po nt=4, Radius=.395, x=3.884, y=0.7325\$

\$po x= 3.924 ,y= 0.681 \$

\$po x= 3.963 ,y= 0.6375 \$

\$po x= 4.002 ,y= 0.5945 \$

\$po x= 4.042 ,y= 0.559 \$

\$po x= 4.081 ,y= 0.5275 \$

\$po x= 4.120 ,y= 0.504 \$

\$po x= 4.160 ,y= 0.488 \$

\$po x= 4.226, y=0.4765 \$

\$po x= 4.239, y=0.4725 \$

\$po x=4.54,y=0.4725\$

\$po x=4.54,y=0\$

\$po x=0,y=0

A.3 Cell-3

University of Twente Third Linac Cell

® KPROB = 1,

ICYLIN=1,

FREQ = 1300,

DX = .02

xdri=2.27,

ydri=2.244,

conv=2.54&

\$po x=0,y=0\$

\$po x=0 ,y= 0.551 \$

\$po x=0.821,y=0.551\$

\$po nt=4, x=.872,y=.602,Radius=.051\$

\$po nt=4, x=.715,y=.759,Radius=.157\$

\$po x=.5672,y=.82508\$

\$po nt=5, x=.341, y=1.1815, Radius=0.394\$

\$po x=.341,y=1.6145\$

\$po x=.341,y=2.244\$

\$po nt=5, x=1.522,y=3.430,Radius=1.181\$

\$po x= 3.018 ,y= 3.430 \$

\$po nt=5, x= 4.199 ,y= 2.244 ,Radius=1.181 \$

\$po x= 4.199 ,y= 1.6145 \$

\$po x= 4.199 ,y= 1.1815 \$

\$po nt=5, x= 3.9728 ,y= 0.82508 ,Radius=.394 \$

\$po x= 3.825 ,y= 0.759 \$

\$po nt=4, x= 3.668 ,y= 0.602 ,Radius=.157 \$

\$po nt=4, x= 3.719 ,y= 0.551 ,Radius=.051\$

\$po x= 4.54 ,y= 0.551 \$

\$po x= 4.54 ,y= 0 \$

\$po x=0,y=0\$

Appendix B: Solenoid Model

University of Twente Solenoid Model

```
&reg kprob=0,      ! Poisson or Pandira problem
mode=-1,          ! Materials have fixed permeability
icylin=1,         ! Cylindrical symmetry
dx=.05,dy=.05,   ! Mesh size intervals
nbslo=1,          ! Dirichlet boundary condition on lower edge
nbsup=0,          ! Dirichlet boundary condition on upper edge
nbslf=0,          ! Dirichlet boundary condition on left edge
nbsrt=0,          ! Dirichlet boundary condition on right edge
conv=2.54,
```

```
ktop=10,ltop=50,
xminf=0,xmaxf=2,yminf=0,ymaxf=20
&
```

```
&po x=0.0,y=0.0 &
&po x=20.0,y=0.0 &
&po x=20.0,y=30.0 &
&po x=0.0,y=30.0 &
&po x=0.0,y=0.0 &
```

; Magnet Iron

```
&reg mat = 3&
```

```
&po y=      5      ,x=      1.1025 &
&po y=      5      ,x=      7.5    &
&po y=     5.78    ,x=      7.5    &
&po y=     5.78    ,x=     5.51    &
&po y=     9.405   ,x=     5.51    &
&po y=     9.405   ,x=     3.4305 &
&po y=     9.778   ,x=     3.4305 &
&po y=     9.778   ,x=     2.4015 &
&po y=     9.405   ,x=     2.4015 &
&po y=      8.6    ,x=     3.385   &
&po y=      8.6    ,x=     3.9825 &
&po y=      5.78   ,x=     3.9825 &
&po y=      5.78   ,x=     2.342   &
&po y=      7.034  ,x=     2.342   &
&po y=      8.6    ,x=     1.693   &
&po y=      9.466  ,x=     1.4695 &
&po y=      9.466  ,x=     1.1025 &
&po y=      5      ,x=     1.1025 &
```

```
;Pipe
&reg mat = 3&
&po y=      6.988 ,x=    5.51  &
&po y=      6.988 ,x=    8.37  &
&po y=     14.937 ,x=    8.37  &
&po y=     14.937 ,x=    5.51  &
&po y=     13.8625 ,x=    5.51  &
&po y=     13.8625 ,x=    7.765 &
&po y=      8.0625 ,x=    7.765 &
&po y=      8.0625 ,x=    5.51  &
&po y=      6.988 ,x=    5.51  &
```

```
;Coil1
&reg mat = 1, cur = 10000&
&po y=      5.78 ,x=    2.342 &
&po y=      8.6 ,x=    2.342 &
&po y=      8.6 ,x=    3.9825 &
&po y=      5.78 ,x=    3.9825 &
;&po y=      5.78 ,x=    2.342 &
```

```
;Coil 2
&reg mat = 1, cur = -30489&
&po y=      8.0625 ,x=    5.51  &
&po y=     13.8625 ,x=    5.51  &
&po y=     13.8625 ,x=    7.765 &
&po y=      8.0625 ,x=    7.765 &
;&po y=      8.0625 ,x=    5.51  &
```

```
&MT mtd = 3,
mu = 1404&
```

Appendix C: PARMELA Input File

run 1 1 1300. -0.001190 .000001 9 .511 938.3 1.022

title

6MeV Injector for U-of-Twente

drift 0 1.1 1

cell 5.765 1.2 1 0. 26. 2 5 -1

sbload 0 1.2 0 5 1 .14057e14 11.658 0.44801e13 .44444

cell 11.53 1.2 1 180. 14.4 4 5 -1 0 0 0

sbload 0 1.2 0 5 1 .14057e14 11.658 0.44801e13 .44444

cell 11.53 1.4 1 0. 10.6 3 5 -1 0 0 0

sbload 0 1.4 0 5 1 .14057e14 11.658 0.44801e13 .44444

cell 11.53 1.4 1 180. 10.6 3 5 -1 0 0 0

sbload 0 1.4 0 5 1 .14057e14 11.658 0.44801e13 .44444

cell 11.53 1.4 1 0. 10.6 3 5 -1 0 0 0

sbload 0 1.4 0 5 2 .14057e14 11.658 0.44801e13 .44444

cell 11.53 1.4 1 180. 10.6 3 5 -1 0 0 0

drift 3.1623 1.2 1

cfield 2

UOF20LHCell1_B.T7

cfield 4

UOF20LFCell1_B.T7

cfield 3

UOF20LFCell2_B.T7

Poisson -24.7 -1.0

UOF20S1.T7

drift 20.91666667 1.2 1

quad 5.5 1.2 1 -299.189723111

drift 20.91666667 1.2 1

quad 5.5 1.2 1 201.008868947

drift 20.91666667 1.2 1

quad 5.5 1.2 1 -225.98611794

drift 20.91666667 1.2 1

quad 5.5 1.2 1 124.889454052

drift 20.91666667 1.2 1

quad 5.5 1.2 1 32.4846842828

drift 20.91666667 1.2 1

wiggler 125 0.8 1 50 10 4282.655 0.707106781 0 0 0

drift 14.5 1.2 1

quad 5.5 1.2 1 871.908

drift 5.0 1.2 1

quad 5.5 1.2 1 -412.676

drift 14.5 1.2 1

rotate 0 1.2 1 -90

bend 4.71238898 1.2 1 6.32 9

bend 4.71238898 1.2 1 6.32 9

bend 4.71238898 1.2 1 6.32 9

bend 4.71238898 1.2 1 6.32 9

bend 4.71238898 1.2 1 6.32 9

bend 4.71238898 1.2 1 6.32 9

bend 4.71238898 1.2 1 6.32 9

bend 4.71238898 1.2 1 6.32 9

bend 4.71238898 1.2 1 6.32 9

bend 4.71238898 1.2 1 6.32 9

rotate 0 5 1 90

drift 50 5 1

zout

charge -1 1

input 9 5000 20. .200 160. 9.36 0

output 5

scheff 3 1. 1.5 50 200 0 0 5

start 40 0.2 5000 1 50

continue 0.2 100000 1 50

end